RESEARCH ARTICLE

WILEY

A poly-superellipsoid-based approach on particle morphology for DEM modeling of granular media

Shiwei Zhao [iD] | Jidong Zhao [iD]

Department of Civil and Environmental Engineering, The Hong Kong University of Science and Technology, Clearwater Bay, Kowloon, Hong Kong

Correspondence
Shiwei Zhao, Department of Civil and Environmental Engineering, The Hong Kong University of Science and Technology, Clearwater Bay, Kowloon, Hong Kong.
Email: ceswzhao@ust.hk

Summary

Particle morphology plays a key role in affecting physical and mechanical behaviors of granular media. While various mathematical approaches and shape descriptors have been proposed to describe the morphological properties of granular particles, it remains a challenge to effectively incorporate them for efficient discrete modeling of granular materials. This study presents a new poly-superellipsoid-based approach for three-dimensional discrete element method (DEM) modeling of non-spherical convex particles. A uniform mathematical description of 3D poly-superellipsoidal surface is employed to represent a realistic granular particle, which is shown to be versatile and effective in reproducing a wide range of shape features (including elongation, flatness, angularity, and asymmetry) for real particles in nature. A novel optimization approach based on hybrid Levenberg-Marquardt (LM) and Gilbert-Johnson-Keerthi (GJK) algorithms is further developed for efficient and robust contact detection in DEM simulation of poly-superellipsoidal assemblies. Simulations of granular packing and triaxial compression tests show that the proposed approach is generally robust and efficient for both dynamic and quasistatic modeling of granular media.

KEYWORDS

contact detection, discrete element method, granular media, particle shape, superellipsoid

1 | INTRODUCTION

Micromechanics-based numerical approaches represented by the discrete element method (DEM)[1] are increasingly popular across many disciplines of engineering and science on capturing the mechanical behaviors of granular materials while providing grain-scale insights.[2-6] In geomechanics applications, DEM users commonly employ idealized spherical discrete elements to simulate granular grains due to the advantages this may offer, including easy contact detection and high computational efficiency.[6-10] However, numerical studies have proven that grain shape underpins various facets of the mechanical responses for granular materials and should be properly accounted for in their modeling.[11-15] Irregular shape of grains, for example, has been found attributable to the increase in particle rotation/rolling resistance, the enhancement of particle interlocking, and hereby the overall strength of a granular material, when compared with simulations with spherical particles.[16,17] Indeed, grain shape may play a key role in forming the fabric structure of a granular assembly[18] and through which the macroscopic responses of the material are affected (see, eg, the stress-force-fabric relationship[19]). A popular indirect way to consider shape effect while using spherical particles for computational efficiency is the

Correction added on 7 August 2019, after first online publication: "CRF Project No. C6012-15G" has been added to the Funding information.

introduction of rolling resistance at interparticle contacts or the so-called rolling resistance model.[20,21] The rolling resistance model indeed helps to gain increased shear strength alone for granular materials but remains ineffective in reproducing other granular behaviors where grain shape has a clear imprint, such as the induced fabric structure, force transmission mechanisms, and deformation characteristics.[22] Therefore, it is sometimes mandatory rather than optional to incorporate grain shapes directly in DEM simulations.

There have been progresses in attempting reconstructing sand grains with realistic shapes based on different mathematical approaches and experimental techniques.[23,24] Image processing techniques, for example, have been developed to reconstruct 3D particles from computed tomography (CT) images of realistic grains, based on which characteristics of particle shape and granular fabric can be analyzed.[25-27] Fourier shape descriptors combined with random fields theory[28] and spherical harmonics[29] have been proposed to characterize the complex shape features associated with a natural grain. These methods have been further used to guide the clumping or clustering of spheres/disks (the clump technique) to generate virtual 3D/2D particles with realistic complex shapes for use in DEM modeling.[30,31] To render sufficient accuracy for fitting the shape characteristics, however, a large number of spheres/disks are needed (approximately 100-400 reported in the literature[28,32]) to form a single clumped particle, which invariably leads to unwanted dramatical increase in computational cost due to orders of magnitude increase in need for contact detection in a DEM simulation.[33] This may limit the total number of clumped particles one can simulate in DEM. To partially alleviate the grief associated with clumped approaches, Lim et al[34] employed a nonuniform rational basis splines (NURBS) approach to represent convex grains for a better computational efficiency. Nevertheless, as mentioned by the authors, the implementation of the contact detection between two NURBS particles remains nontrivial, and a large number of control points are required for complex shapes. More recently, Kawamoto et al[35] proposed a level-set-based approach to handle contact detection of realistic particles akin to using lookup tables with constant time complexity. It has been demonstrated that this approach enables effective and direct DEM modeling of realistic particles that are reconstructed from CT images. Understandably, the lookup table strategy relies crucially on the availability of computer memory and poses stringent demand on the performance of computers to run the contact detection in each DEM simulation step, which may lead to greatly increased computing time or frequent system crashes as reported by the authors.

For practical DEM modeling, there is still a need to weigh a balance between realistic approximation of particle shapes and affordable computational efficiency. This is especially relevant for the majority of DEM modelers who can only access limited computational resources (eg, a multicore workstation at best) but wish to achieve realistic simulation results. While it is widely agreed that particle shape does matter,[36] the degree and extent one should and could reproduce the particle morphology of realistic grains for DEM modeling remains an open issue. To this end, there have been endeavors made on exploring non-spherical particle shapes for DEM modeling in the past decade. Clumping spheres to form a non-spherical shape (ie, the clump technique[31,37]) is probably the most straightforward approach but with apparent drawbacks as mentioned above. Where possible, it is always desirable to use as fewer spheres as possible in the clumping.[38] Polyhedrons have been employed to simulate sand grains in geomechanical applications, eg, direct shear tests[16] and triaxial tests[39] of sands. To simulate sand grains by polyhedrons, the efficiency of contact detection depends stringently on the number of vertices, even with efficient contact detection algorithms such as shortest link method[40] and inner potential particle.[41] Polyhedrons suit well for modeling angular particles, whereas for less angular particles, it is preferable to use implementation-friendly shapes to achieve better computational efficiency. Ellipsoids[42,43] and ovals[44] are among the early pioneering successful attempts in using smooth shapes to capture elongation or flatness of particles. Superellipsoids[18,45] are able to yield a broader range of smoothed particle shapes with control on angularity, elongation, and flatness.

The present study is motivated by a novel method based on poly-ellipsoid,[46,47] which are constructed from pieces of ellipsoids to capture possible skewness of realistic particles. We herein propose a uniform mathematical description of poly-superellipsoidal surface to represent a much broader range of convex particle shapes and capture major shape characteristics, such as flatness, asymmetry, elongation, and angularity. A novel optimization methodology based on hybrid Levenberg-Marquardt (LM)[48] and Gilbert-Johnson-Keerthi (GJK)[49] algorithms is further developed for efficient and robust contact detection of poly-superellipsoidal particles in DEM. As will be demonstrated, the proposed poly-superellipsoid-based approach offers an excellent representation of realistic grain shapes while facilitating efficient and robust DEM simulations for granular media.

This paper is organized as follows: Sections 2 and 3 present the mathematical descriptions of geometry and properties of a poly-superellipsoidal particle. The motion for poly-superellipsoidal particles is briefly introduced for the completeness of presentation in Section 4. A highly robust and efficient algorithm of contact detection for poly-superellipsoids is proposed and validated in Section 5. Demonstrative examples on simulations of granular packing and triaxial compression based on the proposed method are presented in Section 6, followed by the major conclusions drawn from the study in Section 7.
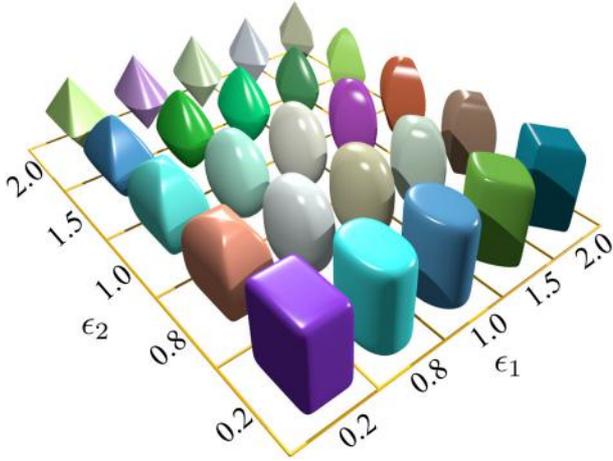
FIGURE 1   Superellipsoids with $r_x = 1.0, r_y = 1.5, r_z = 2$ and varying ϵ_1 and ϵ_2 [Colour figure can be viewed at wileyonlinelibrary.com]

2 | PARTICLE GEOMETRY

2.1 | Superellipsoid

The surface function of a superellipsoid in the local Cartesian coordinates can be defined as[50]

$$\left(\left| \frac{x}{r_x} \right|^{\frac{2}{\epsilon_1}} + \left| \frac{y}{r_y} \right|^{\frac{2}{\epsilon_1}} \right)^{\frac{\epsilon_1}{\epsilon_2}} + \left| \frac{z}{r_z} \right|^{\frac{2}{\epsilon_2}} = 1, \tag{1}$$

where r_x, r_y, and r_z are referred to as the semi-major axis lengths in the direction of x, y, and z axes, respectively, and $\epsilon_i (i = 1, 2)$ are the shape parameters determining the sharpness of particle edges or squareness of particle surface. Similar definitions of a superellipsoid can also be found in Williams and Pentland.[51] Varying ϵ_i between 0 and 2 yields a wide range of convex-shaped superellipsoid as exemplified in Figure 1. A typical parametric function of a superellipsoid surface is given as

$$x = \text{Sign}(\cos\theta)r_x |\cos\theta|^{\epsilon_1} |\cos\phi|^{\epsilon_2}, \tag{2a}$$

$$y = \text{Sign}(\sin\theta)r_y |\sin\theta|^{\epsilon_1} |\cos\phi|^{\epsilon_2}, \tag{2b}$$

$$z = \text{Sign}(\sin\phi)r_z |\sin\phi|^{\epsilon_2}, \tag{2c}$$

where $\theta \in [0, 2\pi)$, $\phi \in \left[-\frac{\pi}{2}, \frac{\pi}{2} \right]$ and $\text{Sign}(x)$ is the signum function.

The surface normal direction of a superellipsoid is another superellipsoid, which is a dual to the original one.[50] Given a normal vector (n_x, n_y, n_z) on the surface, the corresponding local spherical coordinate (θ, ϕ) is obtained through the following relationship:

$$\theta = \text{atan2} \left(\text{Sign}(n_y) |r_y n_y|^{\frac{1}{2-\epsilon_1}}, \text{Sign}(n_x) |r_x n_x|^{\frac{1}{2-\epsilon_1}} \right), \tag{3a}$$

$$\phi = \text{atan2} \left(\text{Sign}(n_z) \left| r_z n_z | \cos(\theta)|^{2-\epsilon_2} \right|^{\frac{1}{2-\epsilon_2}}, |r_x n_x|^{\frac{1}{2-\epsilon_2}} \right), \tag{3b}$$

where $\text{atan2}(x, y)$ is the arctangent function of $\frac{x}{y}$ producing a value in the interval $(-\pi, \pi]$, which can be mapped to $[0, 2\pi)$ by adding 2π to the negative value.

2.2 | Poly-superellipsoid

Motivated by the construction of a poly-ellipsoid proposed by Peters et al,[46] a poly-superellipsoid is constructed by assembling eight pieces of superellipsoids, as shown in Figure 2. The surface of each octant is controlled by Equation (1), and the combination of eight surface functions yields the following surface functions of a poly-superellipsoid:

$$\left(\left| \frac{x}{r_{xi}} \right|^{\frac{2}{\epsilon_{1i}}} + \left| \frac{y}{r_{yi}} \right|^{\frac{2}{\epsilon_{1i}}} \right)^{\frac{\epsilon_{1i}}{\epsilon_{2i}}} + \left| \frac{z}{r_{zi}} \right|^{\frac{2}{\epsilon_{2i}}} = 1, \tag{4}$$

FIGURE 2 A poly-superellipsoid ($r_x^+ = 1.0, r_x^- = 0.5, r_y^+ = 0.5, r_y^- = 2.5, r_z^+ = 0.5, r_z^- = 1.7$ and $\epsilon_1 = \epsilon_2 = 1.0$) in a local coordinate system with origin A, at the geometric center and B, at the mass center. Note: One color stands for one octant [Colour figure can be viewed at wileyonlinelibrary.com]
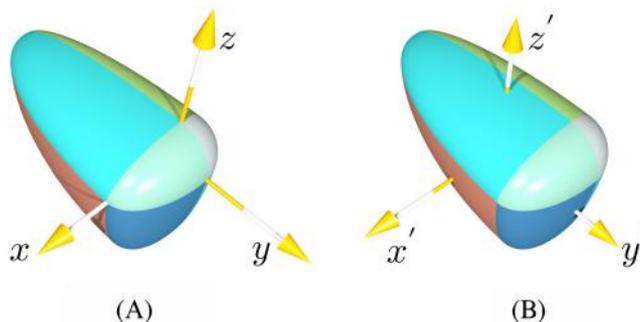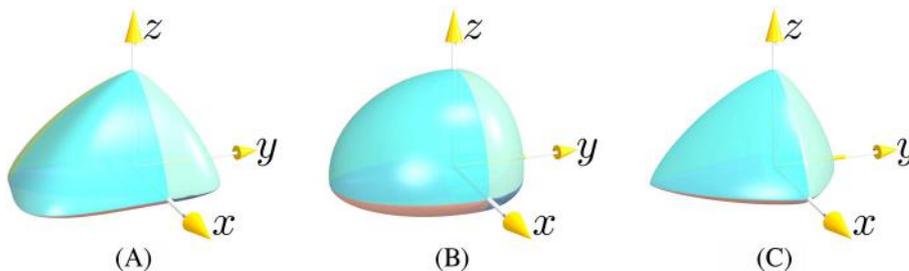

FIGURE 3 Poly-superellipsoids with $r_x^+ = 1.0, r_x^- = 0.5, r_y^+ = 0.8, r_y^- = 0.9, r_z^+ = 0.4, r_z^- = 0.6$ and A, $\epsilon_1 = 0.4, \epsilon_2 = 1.5$, B, $\epsilon_1 = \epsilon_2 = 1.0$, C, $\epsilon_1 = \epsilon_2 = 1.5$ [Colour figure can be viewed at wileyonlinelibrary.com]

where $r_{xi}, r_{yi}, r_{zi}, \epsilon_{1i}, \epsilon_{2i}(i = 1, \ldots, 8)$ are shape parameters of the ith octant, ie, 40 shape parameters in total for a poly-superellipsoid. However, we can reduce these parameters according to a condition of a continuous and smooth surface (C1 continuity) by defining

$$\epsilon_{1i} = \epsilon_1, \quad \epsilon_{2i} = \epsilon_2, \tag{5}$$

and

$$r_{x1} = r_{x4} = r_{x5} = r_{x8} = r_x^+, (x \geq 0), \tag{6a}$$

$$r_{x2} = r_{x3} = r_{x6} = r_{x7} = r_x^-, (x < 0), \tag{6b}$$

$$r_{y1} = r_{y2} = r_{y5} = r_{y6} = r_y^+, (y \geq 0), \tag{6c}$$

$$r_{y3} = r_{y4} = r_{y7} = r_{y8} = r_y^-, (y < 0), \tag{6d}$$

$$r_{z1} = r_{z2} = r_{z3} = r_{z4} = r_z^+, (z \geq 0), \tag{6e}$$

$$r_{z5} = r_{z6} = r_{z7} = r_{z8} = r_z^-, (z < 0). \tag{6f}$$

As a result, only eight parameters in total are indeed needed to control the shape of a poly-superellipsoid, where r_x^+, r_y^+, r_z^+ and r_x^-, r_y^-, r_z^- control the elongation of a particle in the positive and negative of the axes, respectively, and $\epsilon_i(i = 1, 2)$ control the squareness of the surface. By varying ϵ_i, we obtain a difference in the surface of a poly-superellipsoid, referring to Figure 3. With $\epsilon_1 = \epsilon_2 = 1$, the shape is identical to the so-called poly-ellipsoid[46] (see Figures 2 and 3B). With $r_x^+ = r_x^-, r_y^+ = r_y^-, r_z^+ = r_z^-$, the shape is identical to a superellipsoid. For the convenience of discussion, two frame-fixed local Cartesian coordinate systems with parallel axes but different origins are introduced: one is originated at the geometric center shown in Figure 2A and the other at the mass center shown in Figure 2B. A transformation between the two coordinates is readily given as

$$x' = x - x_c, \quad y' = y - y_c, \quad z' = z - z_c, \tag{7}$$

where x_c, y_c, z_c are coordinates of the mass center in the coordinate system XYZ, given in Equation (10). In the following sections, the local coordinate with origin at the geometric center is set by default unless otherwise stated.

Figure 4 shows some examples of particle shapes represented by poly-superellipsoids. Evidently, the proposed poly-superellipsoid-based approach may provide a versatile description of particles with a broad range of shapes. Indeed, it is capable of capturing major shape features of realistic particles (nonconvexity can be approximately captured by clumping several poly-superellipsoids, which is not a focus of this study), including flatness, asymmetry, and angularity. One
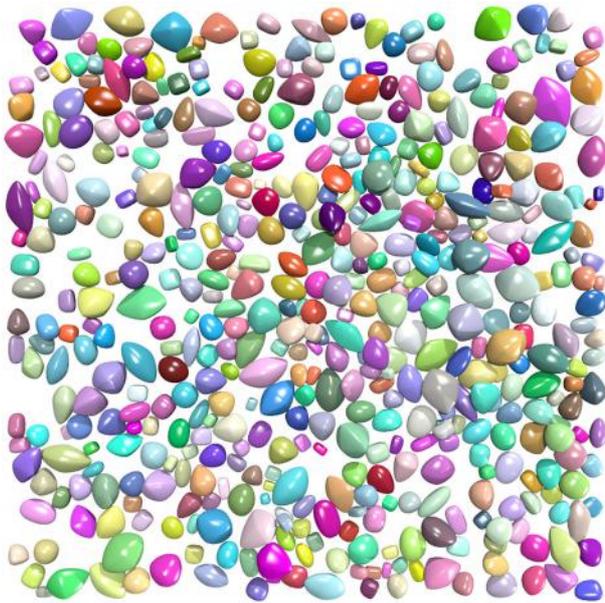
FIGURE 4 Poly-superellipsoids with random values of shape parameters [Colour figure can be viewed at wileyonlinelibrary.com]
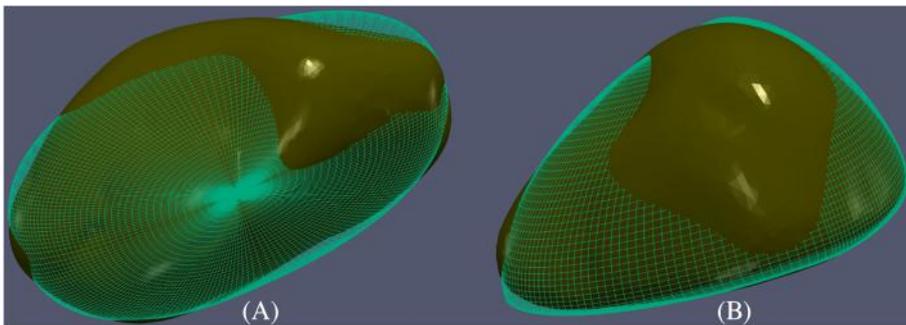

FIGURE 5 Examples of realistic particles (solid) fitted by poly-superellipsoids (wireframe) with A, $\epsilon_1 = 0.85, \epsilon_2 = 1.0, r_x^+ = 3.26, r_x^- = 2.67, r_y^+ = 1.66, r_y^- = 1.59, r_z^+ = 1.81, r_z^- = 1.67$ and B, $\epsilon_1 = 1.1, \epsilon_2 = 1.2, r_x^+ = 2.07, r_x^- = 1.02, r_y^+ = 1.26, r_y^- = 1.23, r_z^+ = 1.40, r_z^- = 0.35$ [Colour figure can be viewed at wileyonlinelibrary.com]

possible way is by fitting point clouds of realistic particles with poly-superellipsoids, which can be done by minimizing the relative error of the inside-and-outside function given below:

$$\min \sum_{k=0}^{N} \left(\left(\left| \frac{x_k}{r_{xi}} \right|^{\frac{2}{\epsilon_1}} + \left| \frac{y_k}{r_{yi}} \right|^{\frac{2}{\epsilon_1}} \right)^{\frac{\epsilon_1}{\epsilon_2}} + \left| \frac{z_k}{r_{zi}} \right|^{\frac{2}{\epsilon_2}} - 1 \right)^2 \right), \tag{8}$$

where N is the number of points and x_k, y_k, z_k are the coordinates of the kth point at the local coordinate system with origin at the geometric center. In general, there are 14 variables in total (eight parameters for particle shape, three for particle center, and the rest three for particle orientation represented by three Euler angles) for fitting an arbitrary point cloud. Solving such a large nonlinear least squares problem with 14 variables may seem daunting but is indeed practically operational. Some preprocessing can be done first to obtain a better initial guess for these variables. For example, the point cloud can be aligned to the principal axes. Moreover, open-source solvers designed for large nonlinear least squares problems, eg, Ceres Solver[52] and IPOPT,[53] can be readily utilized to solve such an optimization problem. The implementation detail is beyond the scope of this paper, which will be not presented for the sake of brevity. Two examples are shown in Figure 5 as a demonstration, where the point clouds are aligned to the principal axes.

2.3 | Support function and support point

Benefiting from the convexity of a poly-superellipsoid, we can construct a one-to-one mapping function $S(\boldsymbol{n})$ from a surface outward normal vector $\boldsymbol{n}(n_x, n_y, n_z)$ to a surface point $\boldsymbol{p}(x, y, z)$ of a poly-superellipsoid with Equations (2a) to (2c) and (3a) and (3b), ie, $\boldsymbol{p} = S(\boldsymbol{n})$. This function yields the furthest point on the surface in the direction of $\boldsymbol{n}$, thus called a support function, which is a convex function. The corresponding furthest point is called a support point, referring to
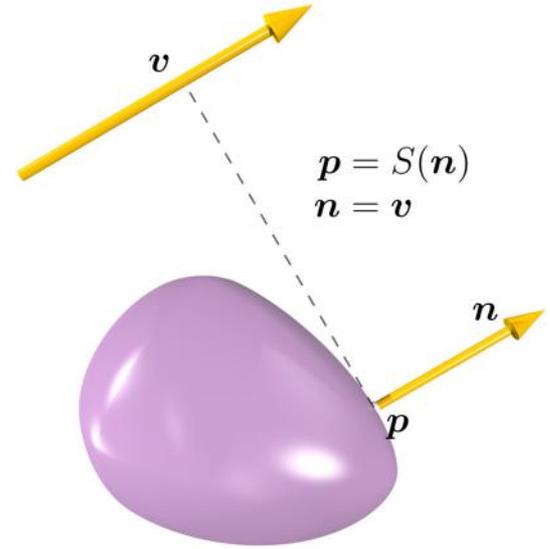
FIGURE 6 A support point p on a particle surface with a given direction vector v and a support function $S(\boldsymbol{n})$. Note: n is the outward normal of particle surface at the support point $\boldsymbol{p}$ [Colour figure can be viewed at wileyonlinelibrary.com]

Figure 6. In mathematics, $S(\boldsymbol{n}) = \sup\{\boldsymbol{n} \cdot \boldsymbol{p}|\boldsymbol{p} \in \Gamma\}$ where Γ is the particle surface. The aforementioned direction vector, ie, $\boldsymbol{v}$ in Figure 6, situates in the particle's local coordinate system, which rotates along with the particle. The particle orientation is tracked by a quaternion $q(q_w, q_x, q_y, q_z) = \cos\frac{\hat{\theta}}{2} + (\hat{e}_x\boldsymbol{i} + \hat{e}_y\boldsymbol{j} + \hat{e}_z\boldsymbol{k})\sin\frac{\hat{\theta}}{2}$, where $\hat{\theta}$ is the angle of the particle rotating around a unit axis $\hat{\boldsymbol{e}}(\hat{e}_x, \hat{e}_y, \hat{e}_z)$. A rotation matrix $\boldsymbol{R}$ can be readily obtained from q so that for a given direction vector $\hat{\boldsymbol{v}}$ in the global coordinate system, the local support point is $S(\boldsymbol{R}^{-1}\hat{\boldsymbol{v}})$, where $\boldsymbol{R}^{-1}$ is the inverse of $\boldsymbol{R}$. The support function $S(\boldsymbol{n})$ will be frequently called upon by Equation (22) during the course of contact detection based on a common normal method, which will be fully introduced in Section 5. For the sake of computational efficiency, it is not necessary to explicitly compute θ and ϕ in Equation (3), so that the support function $S(\boldsymbol{n})$ can be expressed as

$$x = \frac{1}{2}\text{Sign}(n_x)\left[(1 + \text{Sign}(n_x))r_x^+ + (1 - \text{Sign}(n_x))r_x^-\right]\alpha_1^{\epsilon_1/2}\alpha_2^{\epsilon_2/2}, \tag{9a}$$

$$y = \frac{1}{2}\text{Sign}(n_y)\left[(1 + \text{Sign}(n_y))r_y^+ + (1 - \text{Sign}(n_y))r_y^-\right](1 - \alpha_1)^{\epsilon_1/2}(1 - \alpha_2)^{\epsilon_2/2}, \tag{9b}$$

$$z = \frac{1}{2}\text{Sign}(n_z)\left[(1 + \text{Sign}(n_z))r_z^+ + (1 - \text{Sign}(n_z))r_z^-\right](1 - \alpha_2)^{\epsilon_2/2}, \tag{9c}$$

where α_1 and α_2 are equal to $\cos^2(\theta)$ and $\cos^2(\phi)$, respectively, given as follows:

$$\alpha_1 = \begin{cases} \left(1 + \left|\frac{r_y n_y}{r_x n_x}\right|^{\frac{2}{2-\epsilon_1}}\right)^{-1}, & \text{if } n_x \neq 0, \\ 0, & \text{otherwise,} \end{cases}$$

and

$$\alpha_2 = \begin{cases} \left(1 + \left|\frac{r_z n_z}{r_x n_x}\right|^{\frac{2}{2-\epsilon_2}}|\alpha_1|^{\frac{2-\epsilon_1}{2-\epsilon_2}}\right)^{-1}, & \text{if } n_x \neq 0, \\ \left(1 + \left|\frac{r_z n_z}{r_y n_y}\right|^{\frac{2}{2-\epsilon_2}}|1 - \alpha_1|^{\frac{2-\epsilon_1}{2-\epsilon_2}}\right)^{-1}, & \text{else if } n_y \neq 0, \\ 0, & \text{otherwise.} \end{cases}$$

3 | PARTICLE PROPERTIES

The mass center (x_c, y_c, z_c) of a poly-superellipsoid can be obtained by weighing the mass centers of all octants as follows:

$$x_c = \frac{\sum_{i=1}^{8} x_{ci}m_i}{M}, \tag{10a}$$

$$y_c = \frac{\sum_{i=1}^{8} y_{ci} m_i}{M}, \tag{10b}$$

$$z_c = \frac{\sum_{i=1}^{8} z_{ci} m_i}{M}, \tag{10c}$$

with

$$M = \sum_{i=1}^{8} m_i, \tag{11}$$

where M is the mass of the poly-superellipsoidal particle and (x_{ci}, y_{ci}, z_{ci}) and m_i are, respectively, the mass center and the mass of the ith octant, obtained in a closed form as

$$x_{ci} = S_{xi} \frac{3r_{xi}}{4} \frac{B\left(\frac{\epsilon_1}{2}, \epsilon_1\right) B\left(\frac{\epsilon_2}{2}, \frac{3\epsilon_2}{2}\right)}{B\left(\frac{\epsilon_1}{2}, \frac{\epsilon_1}{2}\right) B\left(\epsilon_2, \frac{\epsilon_2}{2}\right)}, \tag{12a}$$

$$y_{ci} = S_{yi} \frac{3r_{yi}}{4} \frac{B\left(\frac{\epsilon_1}{2}, \epsilon_1\right) B\left(\frac{\epsilon_2}{2}, \frac{3\epsilon_2}{2}\right)}{B\left(\frac{\epsilon_1}{2}, \frac{\epsilon_1}{2}\right) B\left(\epsilon_2, \frac{\epsilon_2}{2}\right)}, \tag{12b}$$

$$z_{ci} = S_{zi} \frac{3r_{zi}}{4} \frac{B(\epsilon_2, \epsilon_2)}{B\left(\epsilon_2, \frac{\epsilon_2}{2}\right)}, \tag{12c}$$

with

$$\begin{aligned}
S_{x1} &= S_{x4} = S_{x5} = S_{x8} = 1, \quad S_{x2} = S_{x3} = S_{x6} = S_{x7} = -1, \\
S_{y1} &= S_{y2} = S_{y5} = S_{y6} = 1, \quad S_{y3} = S_{y4} = S_{y7} = S_{y8} = -1, \\
S_{z1} &= S_{z2} = S_{z3} = S_{z4} = 1, \quad S_{z5} = S_{z6} = S_{z7} = S_{z8} = -1,
\end{aligned} \tag{13}$$

and

$$m_i = \frac{1}{12} \rho r_{xi} r_{yi} r_{zi} \epsilon_1 \epsilon_2 B\left(\frac{1}{2}\epsilon_1, \frac{1}{2}\epsilon_1\right) B\left(\frac{1}{2}\epsilon_2, \epsilon_2\right), \tag{14}$$

where ρ is mass density of the material; the term $B(x, y)$ is a beta function defined as

$$B(x, y) = 2 \int_0^{\pi/2} \sin^{2x-1}\phi \cos^{2y-1}\phi d\phi. \tag{15}$$

The principal moments of inertia of an octant superellipsoid are determined by

$$\begin{cases}
I_{xx}^{(i)} = \frac{1}{16} \rho r_{xi} r_{yi} r_{zi} \epsilon_1 \epsilon_2 (r_{yi}^2 \beta_1 + 4r_{zi}^2 \beta_2) \\
I_{yy}^{(i)} = \frac{1}{16} \rho r_{xi} r_{yi} r_{zi} \epsilon_1 \epsilon_2 (r_{xi}^2 \beta_1 + 4r_{zi}^2 \beta_2) , \\
I_{zz}^{(i)} = \frac{1}{16} \rho r_{xi} r_{yi} r_{zi} \epsilon_1 \epsilon_2 (r_{xi}^2 + r_{yi}^2) \beta_1
\end{cases} \tag{16}$$

in which β_1 and β_2 are given as

$$\begin{cases}
\beta_1 = B\left(\frac{3}{2}\epsilon_1, \frac{1}{2}\epsilon_1\right) B\left(\frac{1}{2}\epsilon_2, 2\epsilon_2 + 1\right) \\
\beta_2 = B\left(\frac{1}{2}\epsilon_1, \frac{1}{2}\epsilon_1 + 1\right) B\left(\frac{3}{2}\epsilon_2, \epsilon_2 + 1\right)
\end{cases}. \tag{17}$$

Therefore, the principal moments of inertia of a poly-superellipsoidal particle read as follows:

$$\begin{aligned}
I_{xx}^c &= \sum_{i=1}^{8} I_{xx}^{(i)}, \\
I_{yy}^c &= \sum_{i=1}^{8} I_{yy}^{(i)}, \\
I_{zz}^c &= \sum_{i=1}^{8} I_{zz}^{(i)}.
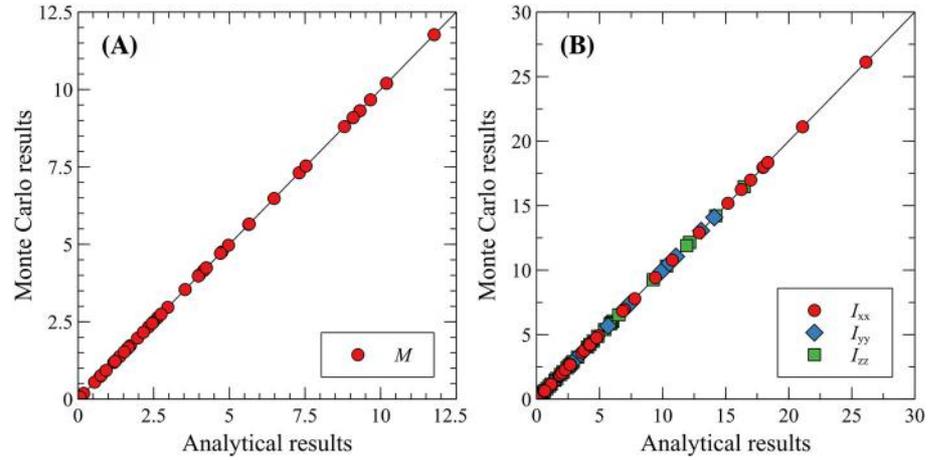\end{aligned} \tag{18}$$

FIGURE 7 Comparison between the Monte Carlo and analytical results of A, mass and B, principal moments of inertia for 50 random poly-superellipsoids [Colour figure can be viewed at wileyonlinelibrary.com]

On the basis of the theorem of parallel axis, the principal moments of inertia in the local coordinate system with origin at the mass center of a poly-superellipsoid are given as

$$
\begin{aligned}
I_{xx} &= I_{xx}^c - (y_c^2 + z_c^2)M, \\
I_{yy} &= I_{yy}^c - (x_c^2 + z_c^2)M, \\
I_{zz} &= I_{zz}^c - (x_c^2 + y_c^2)M.
\end{aligned}
\tag{19}
$$

The particle properties (mass, mass center, and principal moments of inertia) can be numerically integrated with a given function $f(\boldsymbol{x})$ over the whole volume V_{PS} of the poly-superellipsoid based on the Monte Carlo method[54] according to

$$
\boldsymbol{P} = \int_{V_{PS}} f(\boldsymbol{x}) \mathrm{d}v \simeq \frac{V_{box}}{N_p} \sum_{i=1}^{N_p} \xi(\boldsymbol{x}_i) f(\boldsymbol{x}_i),
\tag{20}
$$

where $\{\boldsymbol{x}_i | i = 1, \ldots, N_p\}$ is a set of quasirandom points uniformly distributed within a cuboidal box containing the poly-superellipsoid; N_p is the number of points; V_{box} is the volume of the box; $\xi(\boldsymbol{x}_i)$ is an indicator function, which has a value of 1 if $\boldsymbol{x}_i$ is inside the poly-superellipsoid and 0 otherwise. The function $f(\boldsymbol{x}_i)$ can be ρ, $\rho\boldsymbol{x}_i$, and $\rho||\boldsymbol{x}_i||^2$, yielding an integral $P = M, M\boldsymbol{x}_c, \boldsymbol{I} + M||\boldsymbol{x}_c||^2$, respectively, where ρ is mass density and $M, \boldsymbol{x}_c, \boldsymbol{I}$ are mass, mass center, and moment of inertia, respectively. The mass and principal moments of inertia from the Monte Carlo method are plotted against that from the analytical solution in Equations (11) and (19) in Figure 7, where $N_p = 10^7, \rho = 1$, and $r_x^+, r_x^-, r_y^+, r_y^-, r_z^+, r_z^-$ are randomly selected in [0.01, 5.0] and ϵ_1, ϵ_2 in [0.1, 1.9]. The Monte Carlo and analytical results agree with each other well, suggesting that the analytical solution of particle properties has been correctly formularized.

4 | EQUATION OF MOTION FOR POLY-SUPERELLIPSOIDS

Essential ingredients of DEM have been well documented in the literature, eg, O'Sullivan,[33] which will not be repeated here. For the completeness of presentation, we only briefly introduce the implementation of the poly-superellipsoids in DEM relative to equations of motion. Consider two Cartesian coordinate systems: one is the global $\hat{X}\hat{Y}\hat{Z}$, and the other is the local one $X'Y'Z'$ fixed at the mass center with axes coinciding with the principal axes of inertia so that the moment of inertia tensor is diagonal. Given a particle, its translation and rotation are governed, respectively, by the Newton and Euler equations as follows:

$$
F_i^{(b)} + f_i^{(d)} + \sum_{c=1}^{N} F_i^{(c)} = m \frac{\mathrm{d}v_i}{\mathrm{d}t},
\tag{21a}
$$

$$
T_i^{(d)} + \sum_{c=1}^{N} M_i^{(c)} = I_i \frac{\mathrm{d}\omega_i}{\mathrm{d}t} - (I_j - I_k)\omega_j \omega_k,
\tag{21b}
$$

where i, j, k are subsequent indexes; m is particle mass; v_i and ω_i are the translational velocity of particle mass center and angular velocity around the mass center, respectively; N is the number of contacts; $F_i^{(c)}$ is the contact force at contact c; $F_i^{(b)}$

is the body force; I_i is the principal moment of inertia; $M_i^{(c)}$ is the torque around the mass center at contact c; and $f_i^{(d)}$ and $T_i^{(d)}$ are damping force and damping torque, respectively, which are artificially introduced to facilitate the dissipation of kinetic energy in the system. The Newton equation is solved directly using the so-called leapfrog algorithm[55] at the global coordinate system, while the Euler equation for particle rotation cannot be solved using the aforementioned leapfrog algorithm for non-spherical particles due to the nonequality in the three principal moments of inertia. To facilitate its numerical implementation, quaternions are usually adopted to represent particle orientation and rotation. An extended leapfrog approach proposed by Fincham[56] can further be used to solve particle rotation.

At a given state, the global coordinate $\hat{x}$ of a surface point (ie, the support point at the global coordinate system) of a particle with a specified direction (or normal) $\hat{n}$ is given by

$$\hat{x} = \hat{S}(\hat{n}) = RS(R^{-1}\hat{n}) - x_c + s, \tag{22}$$

where s is the particle position (ie, the mass center of particle) solved from the Newton equation; R is the rotation matrix of a particle from the local coordinate system $X'Y'Z'$ to the global coordinate system $\hat{X}\hat{Y}\hat{Z}$, ie, matrix-represented rotation of the particle solved from the Euler equation and R^{-1} is its inverse transformation; S is the support function at the local coordinate system XYZ, given in Equation (9); and x_c is the mass center at XYZ.

5 | CONTACT AND CONTACT DETECTION

For general contact detection (also called collision detection) of poly-superellipsoids, two sequential phases are considered: broad and narrow detection phases. For the broad contact detection phase, this study adopts the popular sweep and prune algorithm with axis-aligned bounding boxes (AABB) in conjunction with with bounding spheres.[57] In the narrow detection phase, we follow the normal contact concept[45,58] as detailed below.

5.1 | Geometric and mechanical quantities at contact

Given two contacting particles A and B as shown in Figure 8, the two contact points: p^A and p^B, on each of the particle surfaces are determined based on the common normal concept, whereby the outward normals of particle surfaces at p^A and p^B are collinear to the contact normal c. Penetration of the two particles is defined in terms of the contact points as $d = p^A - p^B$, which is employed to compute repulsive force (ie, normal contact force F_n) in the direction of contact normal. A plane orthogonal to the penetration passing through its midpoint (ie, $\frac{1}{2}(p^A - p^B)$) is taken as the contact plane, on which the tangential contact force F_t (ie, sliding friction in usual) acts in an incremental manner but constrained by the Coulomb condition. The magnitudes of F_n and F_t are given as follows:

$$|F_n| = K_n|d|,$$
$$|F_t| = \min\{|F_t' - K_t\Delta u|, \mu|F_n|\}, \tag{23}$$

where K_n and K_t are normal and tangent contact stiffnesses, respectively; F_t' is the previous tangential contact force but rotated to the current contact plane, which is initialized to 0 when two particles contact each other; Δu is the relative displacement on the contact plane during the present time step; and μ is the coefficient of sliding friction.

FIGURE 8 Two contacting particles with exaggerated overlap, after Zhao et al[18] [Colour figure can be viewed at wileyonlinelibrary.com]
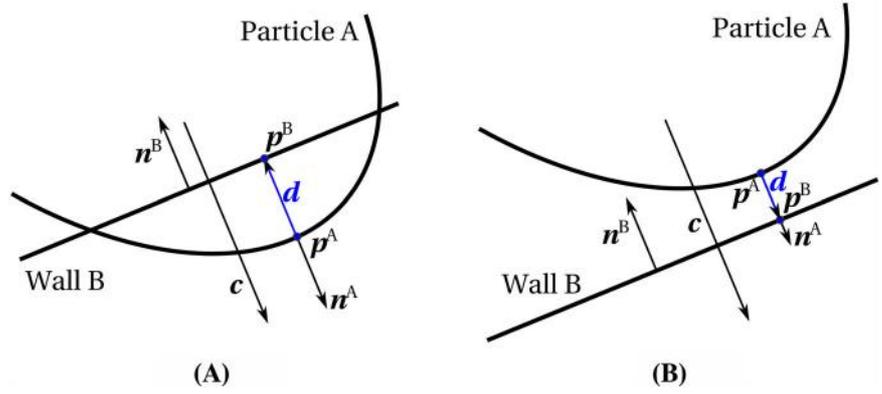
FIGURE 9 Two-dimensional schematic of the contact quantities for A, contacting and B, noncontacting particle-wall pairs [Colour figure can be viewed at wileyonlinelibrary.com]

5.2 | Particle-wall contact

Given a boundary wall B with an outward normal $\boldsymbol{n}^B$, it is generally assumed that particle-wall contact is activated at the side pointed by $\boldsymbol{n}^B$. By virtue of the common normal concept, the contact normal $\boldsymbol{c}$ is identical to the antidirection of $\boldsymbol{n}^B$, shown in Figure 9; thus, the contact point $\boldsymbol{p}^A$ on a given particle A is obtained by the global support function in Equation (22) as

$$\boldsymbol{p}^A = \hat{\boldsymbol{S}}(-\boldsymbol{n}^B). \tag{24}$$

The other contact point $\boldsymbol{p}^B$ can be readily obtained by projecting $\boldsymbol{p}^A$ onto wall B. Therefore, the penetration $\boldsymbol{d} = \boldsymbol{p}^B - \boldsymbol{p}^A$ and other contact quantities are solved. Note that a positive $\boldsymbol{d} \cdot \boldsymbol{n}^B$ corresponds to a valid contact (Figure 9A); otherwise, the particle-wall contact is virtual (Figure 9B). The above description of particle-wall contact detection can be easily extended to particle-facet pairs with marginally additional computational cost by checking whether $\boldsymbol{p}^B$ stays within the facet or not.

5.3 | Particle-particle contact

5.3.1 | Optimization problem

By introducing the common normal concept,[45,58] the outward normal $\boldsymbol{n}^A$ at point $\boldsymbol{p}^A$ shares a common normal with the contact normal $\boldsymbol{c}$, while the outward normal $\boldsymbol{n}^B$ at point $\boldsymbol{p}^B$ has an antidirection of $\boldsymbol{c}$, ie,

$$\boldsymbol{n}^A = -\boldsymbol{n}^B = \boldsymbol{c}. \tag{25}$$

Therefore, considering Equation (25), the contact points are expressed as

$$\boldsymbol{p}^A = \hat{\boldsymbol{S}}^A(\boldsymbol{c}), \quad \boldsymbol{p}^B = \hat{\boldsymbol{S}}^B(-\boldsymbol{c}). \tag{26}$$

The candidate penetration is given as

$$\boldsymbol{d} = \hat{\boldsymbol{S}}^B(-\boldsymbol{c}) - \hat{\boldsymbol{S}}^A(\boldsymbol{c}) = -\hat{\boldsymbol{S}}_{A-B}(\boldsymbol{c}), \tag{27}$$

where $\hat{\boldsymbol{S}}_{A-B}$ is the support function of Minkowski difference between particles A and B. Figure 10 shows the Minkowski difference C of two arbitrary convex shapes A and B, ie, $C = A - B = \{a - b | a \in A, b \in B\}$. Herein, a helpful lemma on Minkowski difference is introduced as follows[59]: as shown in Figure 10A, the Minkowski difference C encloses the origin, suggesting that particles A and B contact with one another and vice versa; while if particles A and B do not have intersection, then the Minkowski difference C does not enclose the origin, and vice versa, as shown in Figure 10B.

Finding the penetration depth $||\boldsymbol{d}||$ can be recast into the following unconstrained optimization problem with contact normal $\boldsymbol{c}$ as a parameter:

$$\min_{\boldsymbol{c}}||\boldsymbol{d}|| = \min_{\boldsymbol{c}}||\hat{\boldsymbol{S}}_{A-B}(\boldsymbol{c})||. \tag{28}$$

The equality of Equation (28) suggests two promising iterative algorithms, ie, the LM algorithm[48] and the GJK algorithm,[49] which can be individually implemented to search the penetration depth. In this work, a hybrid approach of these two algorithms is proposed to achieve a more robust and efficient solution, which is detailed in the following subsection. Furthermore, the candidate penetration $\boldsymbol{d}$ can be regarded as the contact penetration once it shares a common normal with the contact $\boldsymbol{c}$, ie,

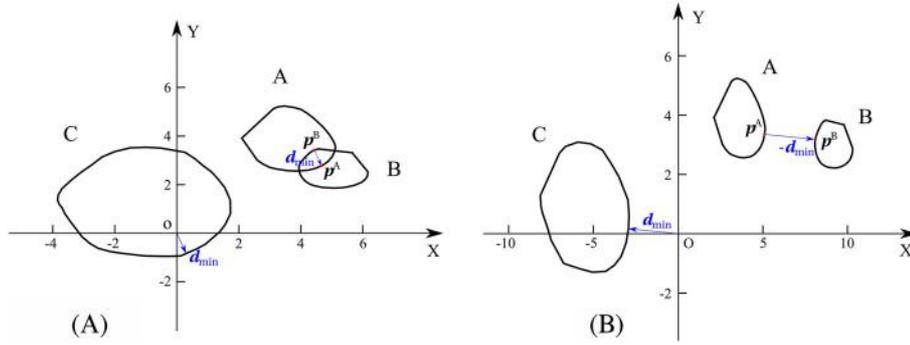$$\boldsymbol{d} \times \boldsymbol{c} = \boldsymbol{0}. \tag{29}$$

FIGURE 10 Two-dimensional schematic of Minkowski difference C of two arbitrary convex particles A and B A, with or B, without contact [Colour figure can be viewed at wileyonlinelibrary.com]

5.3.2 | Hybrid LM and GJK

An efficient approach to solving the optimization problem is needed due to the intensive computational cost during contact detection within a granular system. The LM algorithm,[48] popular for solving nonlinear least-squares problems, is a combination of the steepest decent method and the Newton-Gauss method. To obtain a better performance of the LM algorithm, a scheme of dimensionality reduction for the parameter space is introduced as follows. By introducing a local spherical coordinate system, the contact normal c can be parameterized by two angles: α and β (in radian), ie,

$$c(\alpha, \beta) = \cos \alpha \cos \beta i + \sin \alpha \cos \beta j + \sin \beta k, \tag{30}$$

where i, j, and k are unit base vectors of the global Cartesian coordinate system. Thus, the optimization problem becomes

$$\min_{\alpha,\beta}||d|| = \min_{\alpha,\beta}||\hat{S}_{A-B}(c(\alpha, \beta))||. \tag{31}$$

In implementing the LM algorithm, a finite difference approximation of Jacobian matrix is employed instead of using directly the analytical solution in order to achieve higher implementation and computational efficiency. It is worth noting that Equation (29) is fulfilled when Equation (28) reaches a global minimum.[45] In solving the optimization problem, the following condition will be checked at each iteration,

$$d \cdot c > 0. \tag{32}$$

If this condition is true, the particles are not contacting, referring to the case in Figure 11B. Therefore, we can rule out the consideration of current particle-particle pair and terminate the optimization.

Two important stop criteria are given to guide the convergence of the LM optimization as follows:

$$|d \cdot c| > (1 - \epsilon_l)||d||, \tag{33a}$$

$$\sqrt{(\Delta \alpha)^2 + (\Delta \beta)^2} < \epsilon_m, \tag{33b}$$

where $\Delta \alpha$ and $\Delta \beta$ are the searching steps in the parameter space and ϵ_l and ϵ_m are parameters controlling the accuracy. The penetration depth d searched by the LM algorithm is updated as $|d \cdot c|c$.

The LM optimization presented above has a good performance of convergence. Typically, less than 10 iterations are required to achieve a good convergence for general cases. However, special attention should be paid to two extreme cases where the optimization of LM may fail or become significantly slow to converge. One occurs when the computed contact point from one particle surface is outside the other particle, and the other extreme case is that the LM converges with extremely small steps (eg, 10^{-5} rad for very flat face-to-face contacts). To handle these two issues possibly encountered in the proposed approach, the GJK algorithm[49] is adopted. We coin a name of the proposed approach as a hybrid approach of LM and GJK algorithms.

The GJK algorithm is an efficient algorithm for contact detection of convex bodies and has been popularly applied in computer games and graphic simulations.[59] The general GJK algorithm is used to test whether two convex bodies intersect or not by constructing a sequence of simplexes within the Minkowski difference, $C = A - B$, of the given two bodies. A support function and a simplex are the key ingredients of the GJK algorithm. With the help of a support function, the
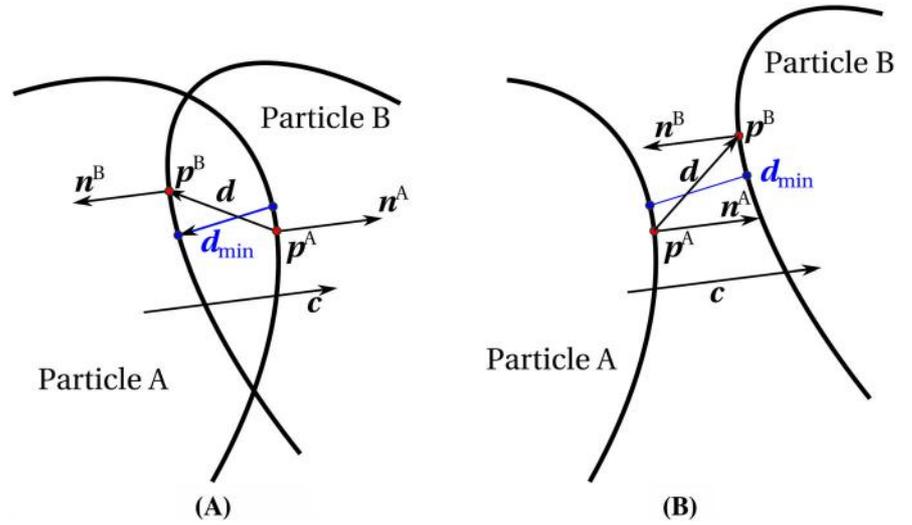
FIGURE 11 Two-dimensional schematic of the optimization solving for A, contacting and B, noncontacting particle-particle pairs [Colour figure can be viewed at wileyonlinelibrary.com]
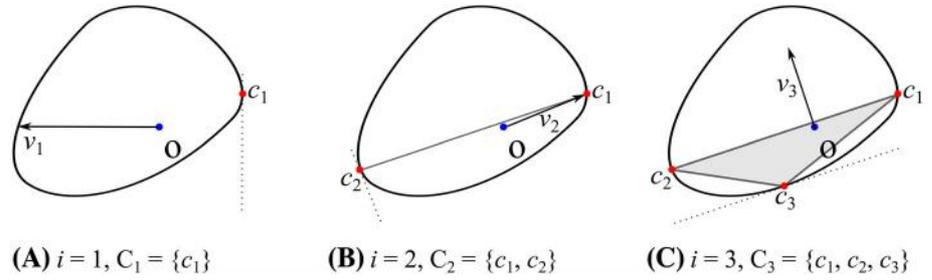

FIGURE 12 Two-dimensional illustration of Gilbert-Johnson-Keerthi (GJK) iterations for Minkowski difference enclosing the origin [Colour figure can be viewed at wileyonlinelibrary.com]

Minkowski difference can be readily computed for a given searching direction. A simplex has at most four vertices located on the boundary of Minkowski difference C, and it can be a point, a line segment, a triangle in 2D, or a tetrahedron in 3D. The kernel of the GJK algorithm is to iteratively find a point nearer the origin on the updated simplex. A brief description on how the GJK algorithm works is given as follows. In each iteration, given a searching direction v_i, a support point c_i can be found via the supporting function $\hat{S}_{A-B}(-v_i)$, which is added to the previous simplex for updating the simplex C_i. Taking a two-dimensional case shown in Figure 12 as an example, an arbitrary searching direction v_1 is given to yield the initial simplex $C_1 = \{c_1\}$ at the first iteration in Figure 12A; at the second iteration $i = 2$ in Figure 12B, the searching direction is updated as v_2, the direction giving the shortest distance between the previous simplex C_1 and the origin. Then, an updated simplex $C_2 = \{c_1, c_2\}$ is obtained. The iteration ends up with the origin being enclosed by the simplex for two contacting particles, as shown in Figure 12C. In general, the GJK algorithm converges fast to find a simplex enclosing the origin for the Minkowski difference C enclosing the origin, ie, for two contacting particles. However, the GJK does not provide the shortest distance directly for two contacting particles. Often, an algorithm called expanding-polytope algorithm (EPA)[59] is adopted to iteratively approximate the shortest distance in a similar manner as the GJK. The EPA is, however, computationally expensive, which will not be considered in this study.

Given that particle penetration encountered in general DEM simulations is sufficiently small—a precondition of the "soft-ball" approach in DEM—we propose a scheme of shape erosion to help for computing penetration depth. As shown in Figure 13A, the particle shape is eroded inward for a small distance δ_r along the inward normal of particle surface so that the eroded shapes of two contacting particles are separated, referring to Figure 13B. In this way, the penetration depth d' can be obtained by the GJK algorithm for two noncontacting particles in a similar manner as that for contacting particles (see Figure 14). The GJK algorithm terminates when achieving a certain accuracy, ie,

$$||\boldsymbol{v}_i||^2 - \boldsymbol{v}_i \cdot \boldsymbol{c}_i < \epsilon_c ||\boldsymbol{v}_i||^2, \tag{34}$$

where $\boldsymbol{v}_i$ is the point within the simplex C_i that is closest to the origin. As a result, the two closest points: $\boldsymbol{p}^{A'}$ and $\boldsymbol{p}^{B'}$, from the two eroded particle surfaces are available, and the contact points $\boldsymbol{p}^A$ and $\boldsymbol{p}^B$ are given as

$$\boldsymbol{p}^A = \boldsymbol{p}^{A'} + \delta_r^A \boldsymbol{c}, \quad \boldsymbol{p}^B = \boldsymbol{p}^{B'} - \delta_r^B \boldsymbol{c}, \tag{35}$$
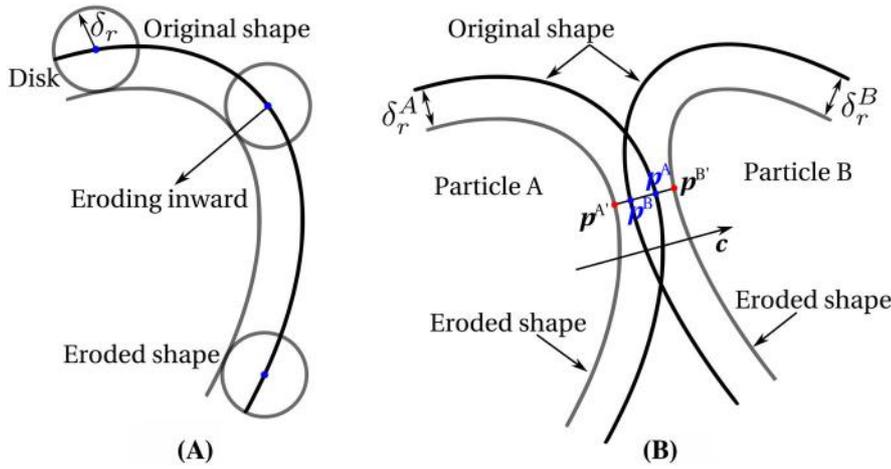
FIGURE 13 Two-dimensional schematic of A, shape erosion with a small disk (sphere in 3D) and B, two contacting particles with eroded shapes [Colour figure can be viewed at wileyonlinelibrary.com]
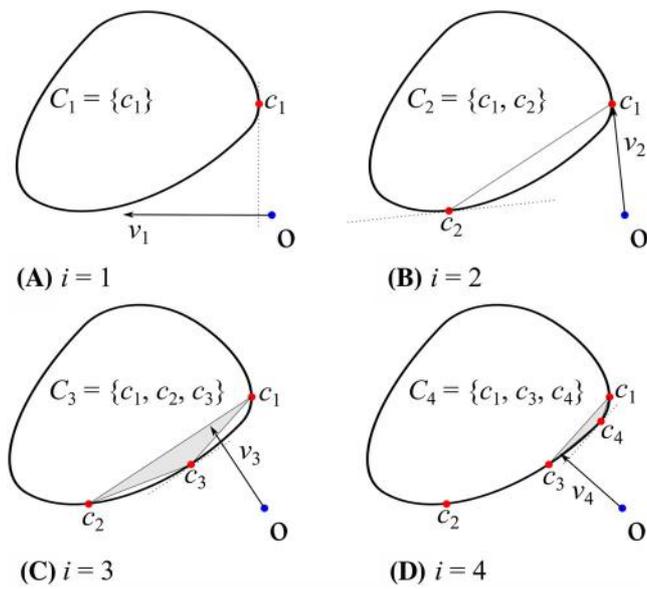

FIGURE 14 Two-dimensional illustration of Gilbert-Johnson-Keerthi (GJK) iterations for Minkowski difference not enclosing the origin [Colour figure can be viewed at wileyonlinelibrary.com]

with

$$c = -\frac{v}{||v||}, \tag{36}$$

where δ_r^A and δ_r^B are erosion distances of the two particles A and B, respectively; c is contact normal; and v is the point closest to the origin from the latest simplex.

With Equations (30) and (36), the parameters α and β in the LM can be readily switched from/to the parameter v in the GJK, resulting in a seamless combination of these two algorithms. Moreover, the contact normal c in the current frame can be cached and taken as the initial guess for the next frame during the course of a DEM simulation, which saves computational time.

5.3.3 | Validation and efficiency analysis

In this section, the validation of the proposed hybrid approach of LM and GJK is conducted, followed by some efficiency analysis and discussion. Two kinds of axis-wise descriptors of particle shape, namely, elongation (l_x, l_y, l_z) and eccentricity (e_x, e_y, e_z), are introduced to assist generating random particle pairs. They are defined along each major axis in such a manner that

$$r_x^+ = l_x e_x, r_x^- = l_x(1 - e_x), r_y^+ = l_y e_y, r_y^- = l_y(1 - e_y), r_z^+ = l_z e_z, r_z^- = l_z(1 - e_z). \tag{37}$$

Three groups of particle shape parameters are listed in Table 1, in which each shape parameter is randomly selected from a given interval. A random particle pair with random shapes but a specified penetration depth d is generated by the following protocol: (a) particle A is located at the origin without rotation (ie, the rotation matrix is identity matrix); (b) a contact normal c is randomly set so that the contact point p^A from particle A is determined by the support function $\hat{S}^A(c)$,

TABLE 1 Three groups of particle shape parameters

Group	Shape	ϵ_1, ϵ_2	Elongation l_x, l_y, l_z	Eccentricity e_x, e_y, e_z
Group 1	Poly-superellipsoid	[0.4, 1.6]	[0.5, 2.0]	[0.2, 0.8]
Group 2	Superellipsoid	[0.4, 1.6]	[0.5, 2.0]	[0.5, 0.5]
Group 3	Ellipsoid	[1.0, 1.0]	[0.5, 2.0]	[0.5, 0.5]
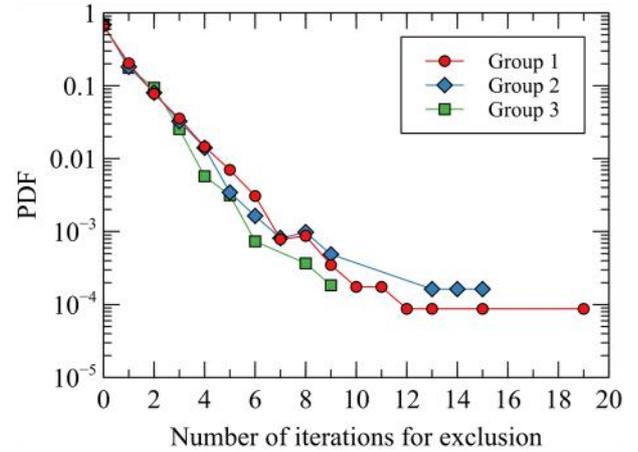
FIGURE 15 Probability distribution function (PDF) of number of iterations needing to exclude two noncontacting particles [Colour figure can be viewed at wileyonlinelibrary.com]

and the contact point p^B from particle B can be computed by $p^B = p^A - dc$; and (c) with a random rotation matrix, the position of particle B is readily obtained by Equation (22).

The performance of the proposed hybrid approach in handling noncontacting particles is examined here. For each of the three groups of particle shape parameters, 10^4 random particle pairs are generated with the penetration depth d randomly selected from $[-0.25, 0]$ (the negative penetration depth means a real distance between the two noncontacting particles). The number of iterations needing to exclude a particle pair is recorded, and the corresponding probability distribution functions (PDFs) are shown in Figure 15 for the three groups. It is worth noting that the AABB combined with a bounding sphere with a radius of $\max\{r_x^+, r_x^-, r_y^+, r_y^-, r_z^+, r_z^-\}$ is utilized to possibly rule out these noncontacting particle pairs but its contribution to the exclusion of particle pairs is not included in the PDFs. As can be seen in Figure 15, the proposed hybrid approach is efficient in ruling out a non contacting particle pair, where the probabilities of exclusion needing zero iteration are 0.657, 0.684, and 0.695, respectively, for groups 1, 2, and 3. It is also evident that almost 97% of particle pairs can be excluded within only three iterations. Moreover, such a good performance suggests that the initial guess of contact normal using the mass center-joining vector is reasonable.

Exact contact detection for contacting particle pairs is much more computationally expensive. Another three groups of tests with the aforementioned random particle pairs but different penetration depth d randomly selected from $[0, 0.01]$ are performed. The parameters for convergence in Equations (33) and (34) are set by trial and error as follows: $\epsilon_l = 0.05$, $\epsilon_m = 1\times10^{-5}$, $\epsilon_c = 1\times10^{-3}$ (by which a good performance in convergence and accuracy is reached as analyzed in the following). In order to quantify the optimization error, two dimensionless quantities, namely, relative error of contact point α_{cp} and relative error of penetration depth α_d, are introduced as

$$\alpha_{cp} = ||p'_c - p_c||/r, \quad \alpha_d = |d' - d|/d, \tag{38}$$

where p'_c and p_c are the solved contact point and the accurate contact point, respectively; r is the average of $r_x^+, r_x^-, r_y^+, r_y^-, r_z^+, r_z^-$ of the two contacting particles; and d' and d are the solved penetration depth and the accurate penetration depth, respectively. Cumulative distribution functions (CDFs) of the relative errors α_{cp} and α_d are shown in Figure 16 for the three groups of tests. It can be seen that almost 95% of solutions have a relative error of less than 1×10^{-3} for both contact point and penetration depth. Such a negligibly small relative error is acceptable for general DEM simulations. Besides, the irregularity in particle shape is likely to increase the optimization error, but on average, it is insignificant. Moreover, the computational cost in terms of number of iterations is recorded, referring to Figure 17A. It appears that only five iterations are needed on average for achieving the aforementioned accuracy. The computationally most heavy part of the hybrid approach is the frequent call of the support function. In each iteration, the number of calls of the support function is dynamic. Thus, for a better estimation of computational cost, the number of calls of the support function is tracked. As shown in Figure 17B, the cumulative distribution functions (CDFs) of number of calls for the support
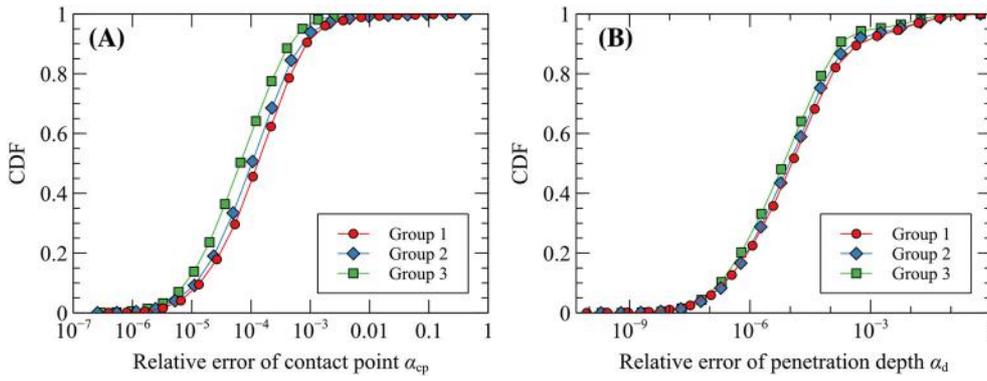
FIGURE 16 Cumulative distribution function (CDF) of relative error of A, contact point α_{cp} and B, penetration depth α_d [Colour figure can be viewed at wileyonlinelibrary.com]
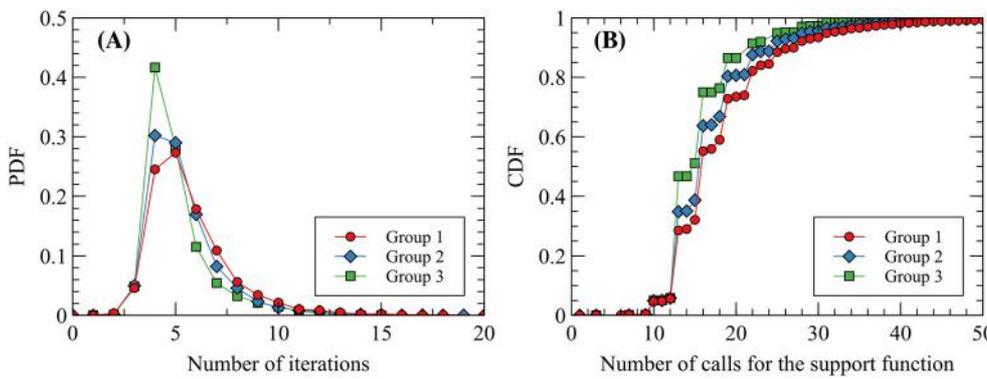

FIGURE 17 A, Probability distribution function (PDF) of number of iterations and B, cumulative distribution function (CDF) of number of calls for the support function after convergence [Colour figure can be viewed at wileyonlinelibrary.com]
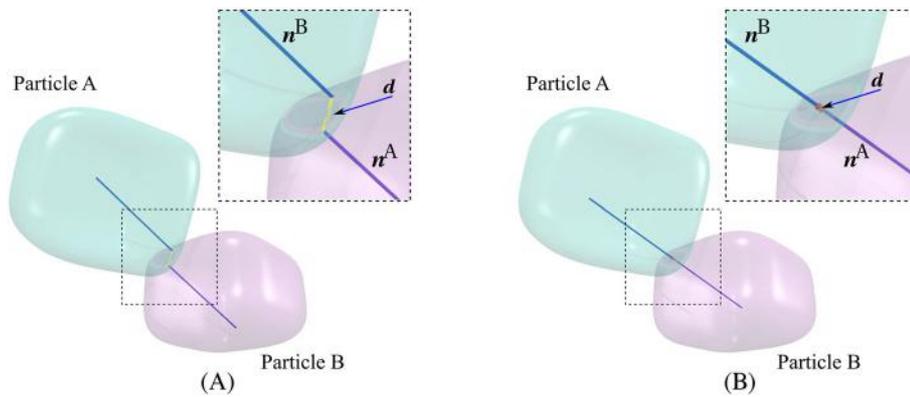

FIGURE 18 Example of two particles with a flat contact: A, the Levenberg-Marquardt (LM) algorithm fails due to slow convergence after 23 calls of the support function; B, the Gilbert-Johnson-Keerthi (GJK) algorithm succeeds after 12 calls of the support function. Note that the initial guess of the contact normal is the vector joining the mass centers of the two particles [Colour figure can be viewed at wileyonlinelibrary.com]

function rapidly increase for the number of calls between 10 and 20, suggesting that the support function is usually called in such a frequency. Besides, it also can be seen that almost 95% of particle pairs need at most 30 calls of the support function. In summary, it can be said that the average number of calls of the support function does not exceed 20. This average upper bound of computational cost is helpful to compare the efficiency between the proposed hybrid approach and others, eg, the clumped technique adopted in multisphere model. However, it is worth mentioning that the performance can be significantly improved with the cached contact normal from the previous frame, which is implemented in our model indeed.

The LM algorithm with a scheme of dimensionality reduction is generally more efficient than the GJK algorithm with a scheme of shape erosion for searching the penetration depth of two contacting particles. However, for some special cases, eg, a flat face-face contact, as shown in Figure 18, the LM algorithm gets stuck into an awkward situation with small searching steps in the parameter space and performs not so well as expected in comparison with the GJK algorithm. However, the proposed hybrid approach of the LM and the GJK is highly robust and efficient. Benefiting from that both LM and GJK are iterative algorithms, the contact normal c at the previous DEM time step can be taken as the searching start of the current time step. Since the time step is usually sufficiently small, the particle motion between two time steps is so small that the current contact normal experiences a rather small deviation from the previous one. Thus, taking the
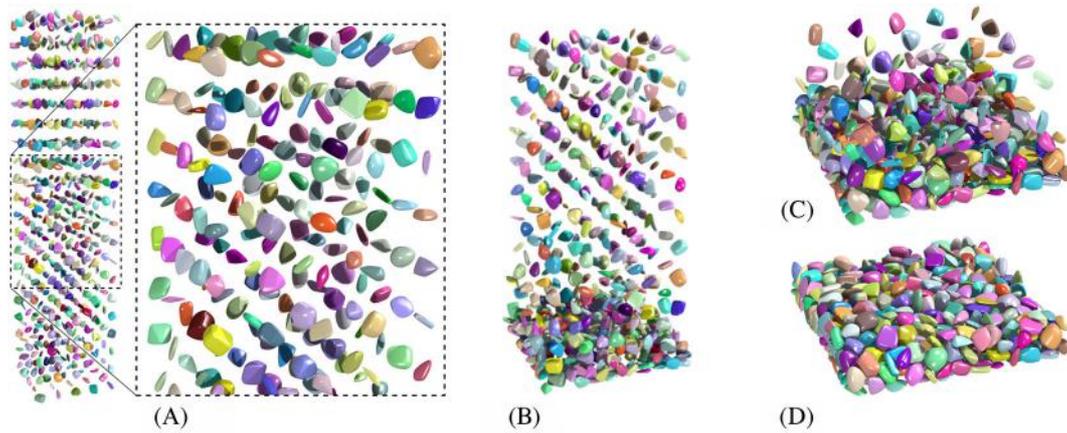
FIGURE 19 Five hundred poly-superellipsoids falling under gravity: A, initial packing, B, after 15 000 time steps, C, after 20 000 time steps, D, after 35 000 time steps. Note: The box is not shown for a better visualization [Colour figure can be viewed at wileyonlinelibrary.com]

previous contact normal as a reasonable initial guess of the current one for optimization can achieve a better performance in general.

6 | SIMULATIONS

The proposed poly-superellipsoid-based method has been implemented in an open-source DEM code the authors developed, SudoDEM,[17,18,60] inheriting a basic framework of YADE.[61] In this section, several examples are employed to demonstrate the robustness and efficiency of the proposed methods in conjunction with the hybrid contact detection algorithm in solving problems relevant to granular media. The cases we choose include granular packing of non-spherical particles and quasistatic triaxial compression tests under both dynamic and quasistatic conditions.

6.1 | Granular packing of non-spherical particles

Random packing of granular materials may find many useful engineering and industrial applications. A packing of granular materials can be formed under different conditions, for example, free falling under gravity, tapping, and vibration. A simulation of granular packing with poly-superellipsoidal particles through free falling into a cubic box ($1 \times 1 \times 4$ m) under gravity is performed using the proposed method in previous sections. In the simulation, 500 particles with random orientations are first positioned at a 5-by-5-by-20 grid shown in Figure 19A, where the parameters of particle shape are randomly selected as $\epsilon_1, \epsilon_2 \in [0.4, 1.6]$, $l_x = 0.1$ m, $l_y, l_z \in [0.02, 0.1]$ m, $e_x, e_y, e_z \in [0.2, 0.8]$. The material properties of particles are set as follows: the material density is set to 2650 kg/m³; the normal and tangential contact stiffnesses are set to 1×10^5 and 7×10^4 N/m, and the coefficient of friction is set to 0.1. All walls of the box are frictionless and have a stiffness one order of magnitude larger than that of the particles. During the simulation, a damping coefficient of 0.3 and a time step of 5×10^{-5} seconds are considered. Note that the aforementioned numerical parameters do matter for the internal structure (or fabric) of granular packing, which deserve a systematic calibration if one wishes to prepare a sample comparable with experiments. Nevertheless, the focus is placed herein upon demonstrating the versatility of the proposed approach and the robustness of the corresponding contact algorithms. Thus, the chosen values of parameters have been based on our experience only.

Figure 19 shows the simulation after 0, 15 000, 25 000, and 35 000 time steps. During the course of packing under gravity, the free particles impact the top of a packing sequentially, and particles may collide with their neighbors (particles or walls) and bounce back and forth. Simulations of free falling of particles have been also adopted by other researchers[40,41] to test the robustness of their DEM algorithms in terms of numerical convergence. The variation of the energy of particles during packing is recorded in Figure 20, where the kinetic energy is $\sum(m_i v_i^2/2 + I_i \omega_i^2/2)$ and the total mechanical energy includes the kinetic energy and the gravitational potential energy defined as $\sum(m_i g h_i)$ (h is the height of particle mass center from the box bottom).

Another popular approach for generating random packing in DEM is the so-called expansion technique akin to the Lubachevsky-Stillinger algorithm for hard particles.[62] In this method, the particles are gradually expanded with a growing rate in the absence of gravitational force. Another simulation of random packing is performed as follows based on the
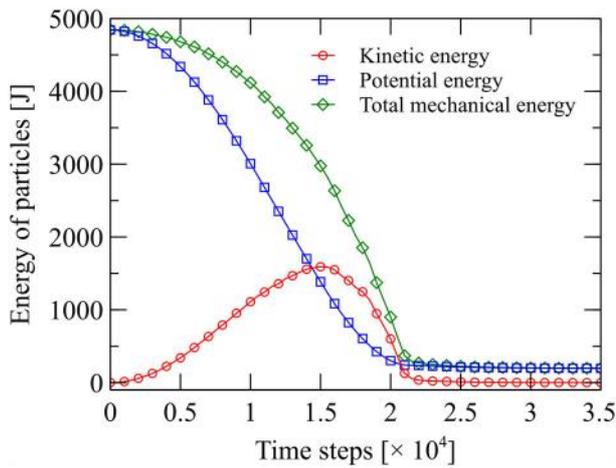
FIGURE 20 Variations of kinetic, potential, and total energy of particles during the packing [Colour figure can be viewed at wileyonlinelibrary.com]
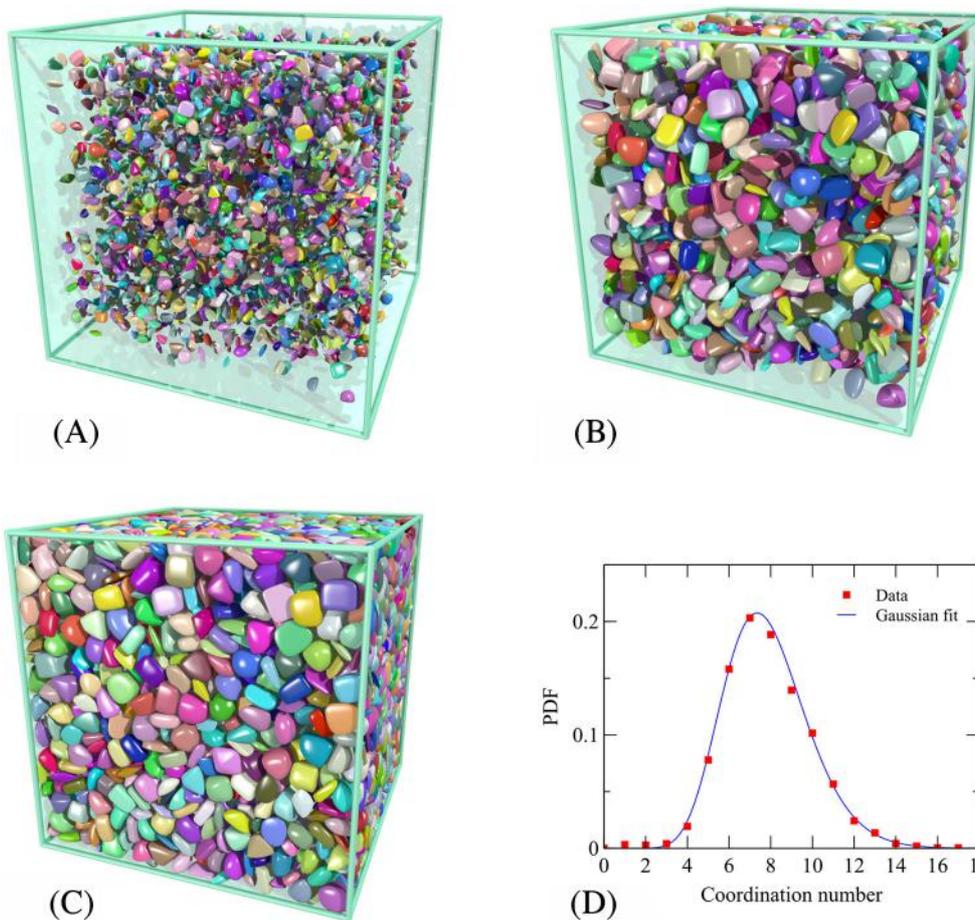

FIGURE 21 A, Initial packing with randomly positioned particles; B, packing after particles expand to the target size; C, packing after isotropic consolidation; D, probability distribution function (PDF) of coordination number within the packing in (C) [Colour figure can be viewed at wileyonlinelibrary.com]

expansion method to further assess the robustness of the proposed algorithms. All numerical parameters have the same values as the free-falling simulation.

(a) First, 5000 poly-superellipsoids with random shapes are generated and randomly positioned within such a cubic box with adequate space to hold them (a void ratio of 0.65 is selected here for a relatively loose packing). There may be some exaggerated or even unreasonable intersections for some particle pairs in the initial packing. This issue can be handled by the following procedure. Prior to performing DEM cycling, all particles are shrunk to their half sizes for a sparse initial packing as shown in Figure 21A. Next, the particles expand with a growing rate until reaching their origin sizes (Figure 21B). During the course of particle expansion, particle velocities are periodically reset to 0 to avoid excessively large velocities due to possible significant penetrations and collisions.

(b) The packing is further subjected to more DEM cycles to reach a state of mechanical equilibrium. Most often, a confining stress is applied to an assembly to achieve a desired isotropic or anisotropic stress state (similar to consolidation in laboratory). This can be done through the so-called numerical stress-controlled servo mechanism, ie, adjusting positions of the confining walls to maintain a constant stress on the boundary until a state of mechanical equilibrium is reached. Figure 21C shows a consolidated packing with a confining stress of 10 kPa. The corresponding void ratio and mean coordination number are 0.501 and 7.834, respectively. And the probability distribution of coordination number is shown in Figure 21D.

It is also instructive to examine how efficient the proposed method as a whole performs for the entire simulation, though the efficiency of contact detection for a single particle pair has been investigated in Section 5.3.3. On the basis of the consolidated packing shown in Figure 21C, 1000 time steps are executed, and the needed computational time is recorded every 100 time steps. To benchmark the computational time of the proposed method, another dense packing of 5000 conventional spherical particles with radii uniformly distributed in [0.02, 0.1] is prepared according to the same procedure as for the poly-superellipsoids. The two packings have a comparable mean coordination number (7.788 for the sphere packing). Note that the contact detection for the spheres is performed directly via computing the Euclidean distance between two particle centers rather than using our proposed general algorithm for poly-superellipsoids. Simulations run with a single thread on an Ubuntu 18.04 desktop with an Intel i7-6700 CPU (clock speed: 3.40 GHz). The computational time averaged among all interactions over every 100 time steps is plotted in Figure 22A. It can be seen that the simulation using the proposed poly-superellipsoid-based approach is on the order of six to seven times more expensive than that using the conventional sphere elements. However, it is worth pointing out that our approach is more efficient for modeling complex shapes than the clumped-spheres approach commonly used in DEM. Furthermore, simulations based on the proposed approach can be readily speed up via multithread programming using openMP, and the speedup is shown in the inset of Figure 22A. As is shown, the performance of speedup is dependent on the total number of particles and contacts, which is not linear. Figure 22B shows the weight of computation time by different DEM processes for poly-superellipsoids and spheres with a single thread. It can be seen that the contact computation (CC) takes an overwhelming fraction of DEM running time. The weight of computation time by CC increases from approximate 90% of spheres to 97% of poly-superellipsoids, and the weight of computation time by integration of particle motion maintains almost constant. Interestingly, the weight of computation time by broad phase of contact detection shows a decrease trend with DEM cycling. One direct explanation is that the neighbor lists are well established after certain DEM cycles, so that it becomes more efficient to traverse particles in the neighbor lists instead of the whole assembly when conducting broad phase of contact detection.

FIGURE 22 A, The single-thread computation time averaged among all interactions over every 100 time steps for poly-superellipsoids and spheres; Inset: speedup of simulations with multithreads parallelized by OpenMP; B, the weight of computation time by different discrete element method (DEM) processes for poly-superellipsoids and spheres with a single thread, BP: broad phase for contact detection; CC: contact computation including the narrow phase for contact detection and computation of contact geometry and forces; Int.: integration of particle motion [Colour figure can be viewed at wileyonlinelibrary.com]
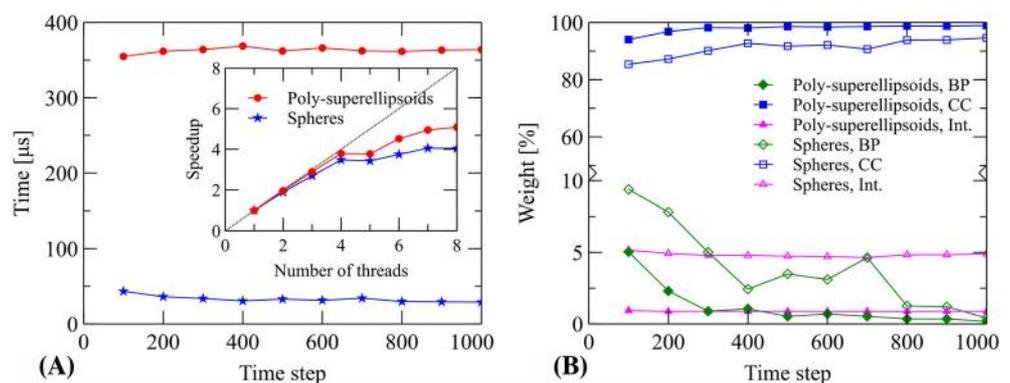
6.2 | Triaxial compression of non-spherical particles

Four cubic specimens containing particles of different shapes, ie, spheres, ellipsoids, superellipsoids, and poly-superellipsoids, with shape parameters randomly selected in the range listed in Table 2, are prepared after consolidation at a confining stress of 100 kPa. Each specimen consists of 5000 particles with a grain size distribution similar to Ottawa 20 to 30 sands shown in Figure 23, where the equivalent diameter stands for the diameter of a sphere with an identical volume. The void ratio of a specimen can be controlled by setting different interparticle coefficient of friction μ_p during the consolidation.[7] It is assumed that the packing with frictionless particles may reach the densest state. We note here that this assumption is reasonable for making the results comparable, even though the approach is not consistent with the standard laboratory tests. Without interparticle friction, three dense specimens of spheres, ellipsoids, and superellipsoids are prepared with a void ratio of 0.633, 0.583, and 0.481, respectively, while a medium-dense specimen of poly-superellipsoids is prepared with frictional particles, $\mu_p = 0.2$, with a void ratio of 0.502. The material properties are set as follows[60]: the normal contact stiffness k_n and the tangential contact stiffness k_t are set as $k_n/\bar{r} = k_t/\bar{r} = 100$ MPa ($\bar{r}$ is the average radius of particles); μ_p is set to 0.3 during shearing, and the mass density 2650 kg/m^3 is scaled up six orders of magnitude to obtained a scaled time step of 1×10^{-5} seconds. During triaxial compression, the top and bottom walls move toward at a constant loading strain rate of 0.01/s (which is sufficiently small to ensure quasistatic shear[60]), whereas the other four side walls move individually to maintain a constant confining stress σ_0 of 100 kPa with the stress-control servo as mentioned above. Compression is terminated at a relative large level of axial strain of 40%, at which a critical state is well observed. Each simulation of the triaxial test runs with a single thread. The simulation for the spherical sample took approximately 2.5 hours, while that for the poly-superellipsoidal, sample took 15 hours or so. Figure 24 shows the configurations of the specimen for poly-superellipsoids at the initial and final states. More details about the triaxial compression procedure are presented in our previous work.[7,60]

The volume-averaged stress tensor[63] calculated from microscopic quantities is adopted to characterize the macroscopic mechanical response of a granular material during shearing, given as

$$\sigma_{ij} = \frac{1}{V} \sum_{c \in V} f_i^c l_j^c, \tag{39}$$

where V is the total volume of the assembly, f^c is the contact force at the contact c, and l^c is the branch vector joining the the centers of the two contacting particles at contact c. On the basis of σ_{ij}, it is ready to obtain the mean stress $p = \sigma_{ii}/3$ and the deviatoric stress $q = \sqrt{3\sigma'_{ij}\sigma'_{ij}/2}$, where σ'_{ij} is the deviatoric part of stress tensor σ_{ij}. The granular deformation is quantified by axial strain ϵ_z and volumetric strain ϵ_v, which can be approximately calculated from the positions of the

Particle Shape	ϵ_1, ϵ_2	Elongation Ratio $l_y/l_x, l_z/l_x$	Eccentricity e_x, e_y, e_z
Poly-superellipsoids	[0.5, 1.4]	[1.0, 1.5]	[0.25, 0.75]
Superellipsoids	[0.5, 1.4]	[1.0, 1.5]	[0.5, 0.5]
Ellipsoids	[1.0, 1.0]	[1.0, 1.5]	[0.5, 0.5]
Spheres	[1.0, 1.0]	[1.0, 1.0]	[0.5, 0.5]

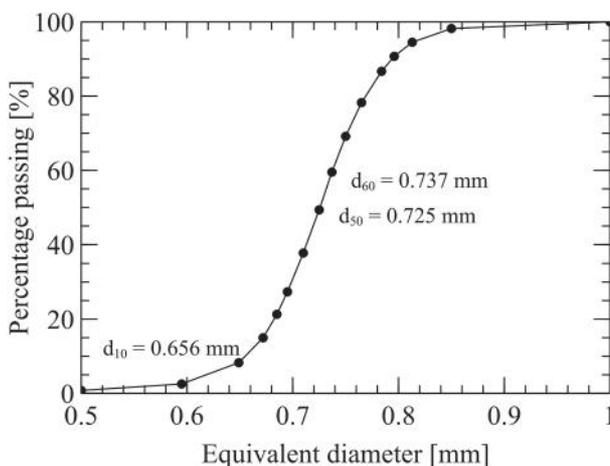TABLE 2 Particle shape parameters for triaxial compression simulations

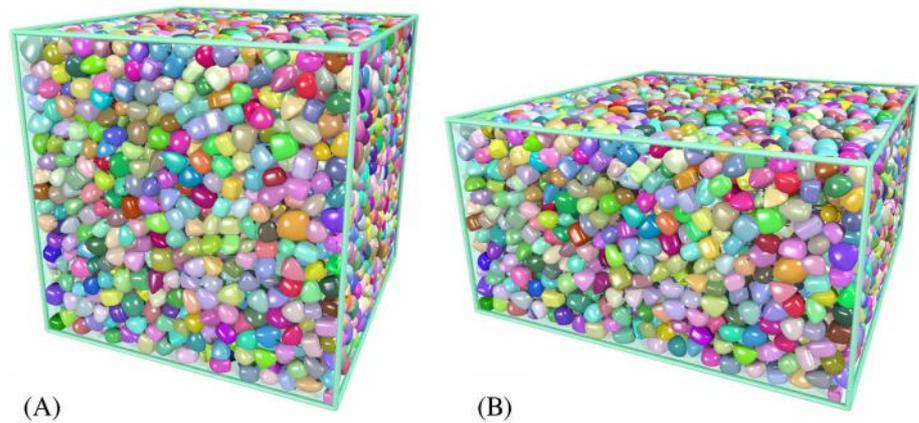

FIGURE 23 Grain size distribution of numerical specimens

FIGURE 24 Configurations of the specimen with poly-superellipsoids at A, the initial and B, the final states. Color is for tracking particle movement intuitively [Colour figure can be viewed at wileyonlinelibrary.com]
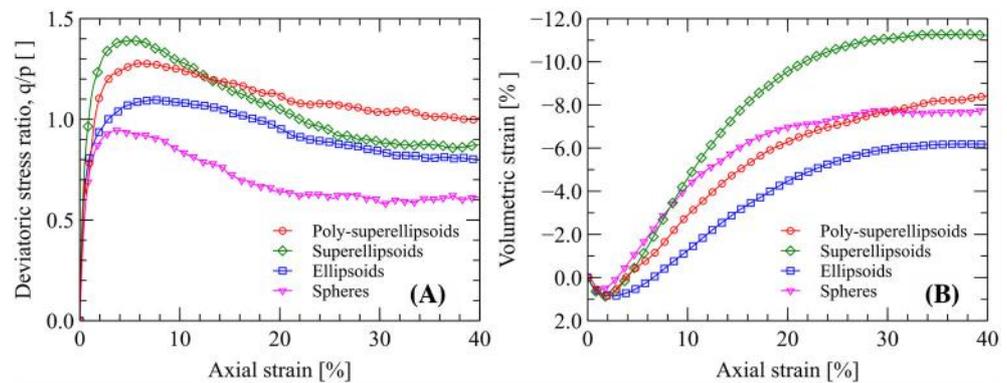

FIGURE 25 Evolution of A, deviatoric stress ratio q/p and B, volumetric strain for specimens with different particle shapes during shearing [Colour figure can be viewed at wileyonlinelibrary.com]

boundary walls, ie, $\epsilon_z = \ln(H_0/H), \epsilon_v = \ln(V_0/V)$, where H and V are the height and volume of the specimen during shearing, respectively, and H_0 and V_0 are their initial values before shear. Negative values of volumetric strain indicate dilation.

Figure 25 shows the evolution of deviatoric stress ratio q/p and the volumetric strain for the four specimens with different particle shapes during shearing. It can be seen that all specimens reach their corresponding critical states in a strain-softening manner with volumetric dilatancy, similar to the behaviors of dense sands well observed in laboratory. For the three specimens with spheres, ellipsoids, and superellipsoids, the deviatoric stress ratio increases with increasing complexity in particle shape shown in Figure 25A. The specimen prepared with superellipsoids exhibits the largest shear strength among all four specimens. However, larger shear strength does not always correspond to more significant dilatancy due to irregularity in particle shape shown in Figure 25B. For example, the specimen of ellipsoids has a considerably enhanced shear strength but relatively lower dilatancy as compared with the specimen of spheres. Moreover, for the specimen of poly-superellipsoids, its peak deviatoric stress ratio is slightly lower than that of the specimen of superellipsoids, which may be attributed to a larger void ratio for the poly-superellipsoid specimen at the initial state compared with the latter. Nevertheless, it is observed that the steady-state deviatoric stress ratio for the specimen with poly-superellipsoids is larger than that for the specimen with superellipsoids, suggesting that DEM modeling of granular media has to take into account of the influence of shape (here, the asymmetric feature characterized by poly-superellipsoids provides additional interlocking among particles compared with the symmetric superellipsoids) in addition to initial void ratio, since the initial fabric structure of granular materials may be greatly affected by the constituent particle shape, which further affects the mechanical granular responses.

It is of interest to further investigate the mechanical responses of these specimens from a microscopic point of view. As a demonstration, emphasis is placed here upon two fabric-and-stress-related quantities, namely, the normal contact force and the coordination number. Normal contact force has been widely regarded as the dominant contributor in undertaking the deviatoric load.[7,17] Coordination number is one of the most commonly used important parameters for characterizing granular fabric and is found sensitive to particle shape.[18] Figure 26 shows the evolutions of mean normal contact force and mean coordination number for the four specimens during shearing. It can be seen that the mean normal contact force exhibits a mild strain-softening trend after the peak, similar to the observation on the deviatoric stress ratio in Figure 25A. However, the mean normal contact force does not show an obvious correlation with complexity of particle shape. For
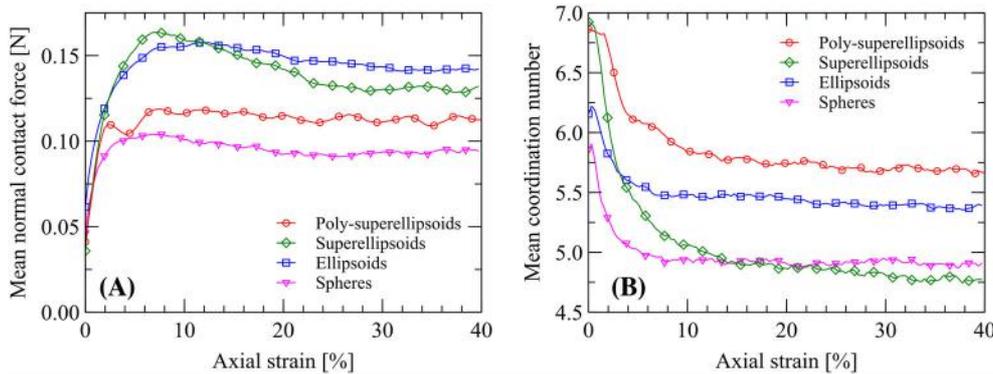
FIGURE 26 Evolution of A, mean normal contact force and B, mean coordination number for specimens with different particle shapes during shearing [Colour figure can be viewed at wileyonlinelibrary.com]

example, the specimen with spheres has the smallest mean normal contact force because of relatively small stress within the assembly, while the specimen with poly-superellipsoids has relatively large stress but small mean normal contact force because of relatively large coordination number. Moreover, the initial mean coordination number increases with increasing complexity in particle shape for the three specimens with the densest states, as shown in Figure 26B. It is also evident that the critical mean coordination number is strongly dependent on particle shape, which significantly affects granular deformation (eg, larger drop in mean coordination number corresponding to larger dilatancy). In addition, the specimen of poly-superellipsoids has a much larger critical coordination number than that of superellipsoids, which to some extent reflects the interlocking enhanced by asymmetry of particles. Further investigation of particle shape effect on the mechanical responses of granular materials is beyond the scope of this paper, which would be conducted as a future study.

7 | CONCLUSIONS

We have proposed new method using poly-superellipsoids for efficient three-dimensional discrete element modeling of granular media in consideration of realistic grain morphology. A robust mathematical description of a poly-superellipsoid needs only eight shape parameters to yield a broad range of convex particle shapes and meanwhile significant computer memory savings compared with other technique, eg, NURBS.[34] The new poly-superellipsoid-based approach is capable of capturing key shape features of realistic granular grains such as sands by fitting CT image data of grains or other possible approaches. On the basis of a common normal concept, novel computational algorithms for contact detection of poly-superellipsoids in DEM modeling have been proposed and further demonstrated to be efficient and straightforward for implementation. The particle-wall contact can be solved efficiently with just one call of the support function, while the particle-particle contact is solved in an iterative manner via a hybrid approach of the LM algorithm and the GJK algorithm. Numerical simulations of granular packing and triaxial compression tests further prove that the proposed hybrid of LM and GJK algorithm is generally valid, robust, and efficient for DEM modeling of poly-superellipsoidal packing. In the demonstrated examples, a linear-spring contact model has been employed for calculation of contact forces. However, other nonlinear contact models, eg, the Hertz-Mindlin model, can be readily implemented as well for poly-superellipsoids, according to a similar procedure for superellipsoids in our previous work.[60]

ORCID

Shiwei Zhao https://orcid.org/0000-0002-3410-3935
Jidong Zhao https://orcid.org/0000-0002-6344-638X

REFERENCES

1. Cundall PA, Strack OD. A discrete numerical model for granular assemblies. *Géotechnique*. 1979;29(1):47-65.
2. Radjai F, Wolf DE, Jean M, Moreau J-J. Bimodal character of stress transmission in granular packings. *Phys Rev Lett*. 1998;80(1):61.
3. Thornton C. Numerical simulations of deviatoric shear deformation of granular media. *Géotechnique*. 2000;50(1):43-53.
4. Nicot F, Darve F. A micro-mechanical investigation of bifurcation in granular materials. *Int J Solids Struct*. 2007;44(20):6630-6652.
5. Nicot F, Xiong H, Wautier A, Lerbet J, Darve F. Force chain collapse as grain column buckling in granular materials. *Granular Matter*. 2017;19(2):18.
6. Sufian A, Russell AR, Whittle AJ. Anisotropy of contact networks in granular media and its influence on mobilised internal friction. *Géotechnique*. 2017;67(12):1067-1080.
7. Guo N, Zhao J. The signature of shear-induced anisotropy in granular media. *Comput Geotech*. 2013;47:1-15.
8. Zhao J, Guo N. Unique critical state characteristics in granular media considering fabric anisotropy. *Géotechnique*. 2013;63(8):695-704.
9. Zhao J, Guo N. The interplay between anisotropy and strain localisation in granular soils: a multiscale insight. *Géotechnique*. 2015;65(8):642-656.
10. Otsubo M., O'Sullivan C., Hanley KJ, Sim WW. The influence of particle surface roughness on elastic stiffness and dynamic response. *Géotechnique*. 2016;67(5):452-459.
11. Shin H, Santamarina J. Role of particle angularity on the mechanical behavior of granular mixtures. *J Geotech Geoenviron Eng*. 2012;139(2):353-355.
12. Payan M, Khoshghalb A, Senetakis K, Khalili N. Effect of particle shape and validity of Gmax models for sand: a critical review and a new expression. *Comput Geotech*. 2016;72:28-41.
13. Alshibli KA, Cil MB. Influence of particle morphology on the friction and dilatancy of sand. *J Geotech Geoenviron Eng*. 2017;144(3):04017118.
14. Xiao Y, Long L, Evans TM, Zhou H, Liu H, Stuedlein AW. Effect of particle shape on stress-dilatancy responses of medium-dense sands. *J Geotech Geoenviron Eng*. 2018;145(2):04018105.
15. Shi X, Herle I, Muir Wood D. A consolidation model for lumpy composite soils in open-pit mining. *Géotechnique*. 2018;68(3): 189-204.
16. Zhao S, Zhou X, Liu W. Discrete element simulations of direct shear tests with particle angularity effect. *Granular Matter*. 2015;17(6):793-806.
17. Zhao S, Zhou X. Effects of particle asphericity on the macro- and micro-mechanical behaviors of granular assemblies. *Granular Matter*. 2017;19(2):38.
18. Zhao S, Zhang N, Zhou X, Zhang L. Particle shape effects on fabric of granular random packing. *Powder Technol*. 2017;310:175-186.
19. Ouadfel H, Rothenburg L. 'Stress–force–fabric' relationship for assemblies of ellipsoids. *Mech Mater*. 2001;33(4):201-221.
20. Jiang M, Shen Z, Wang J. A novel three-dimensional contact model for granulates incorporating rolling and twisting resistances. *Comput Geotech*. 2015;65:147-163.
21. Irazábal J, Salazar F, Oñate E. Numerical modelling of granular materials with spherical discrete particles and the bounded rolling friction model. Application to railway ballast. *Comput Geotech*. 2017;85:220-229.
22. Zhao S, Evans TM, Zhou X. Shear-induced anisotropy of granular materials with rolling resistance and particle shape effects. *Int J Solids Struct*. 2018;150:268-281.
23. Mollon G, Zhao J. Generating realistic 3D sand particles using Fourier descriptors. *Granular Matter*. 2013;15(1):95-108.
24. Lai Z, Chen Q. Reconstructing granular particles from X-ray computed tomography using the TWS machine learning tool and the level set method. *Acta Geotechnica*. 2019;14(1):1-18.
25. Zhou B, Wang J, Wang H. Three-dimensional sphericity, roundness and fractal dimension of sand particles. *Géotechnique*. 2018;68(1):18-30.
26. Nie Z, Wang X, Liang Z, Gong J. Quantitative analysis of the three-dimensional roundness of granular particles. *Powder Technol*. 2018;336:584-593.
27. Sun Q, Zheng J, He H, Li Z. Particulate material fabric characterization from volumetric images by computational geometry. *Powder Technol*. 2019;344:804-813.
28. Mollon G, Zhao J. 3D generation of realistic granular samples based on random fields theory and Fourier shape descriptors. *Comput Meth Appl Mech Eng*. 2014;279:46-65.
29. Wei D, Wang J, Nie J, Zhou B. Generation of realistic sand particles with fractal nature using an improved spherical harmonic analysis. *Comput Geotech*. 2018;104:1-12.
30. Mollon G, Zhao J. Characterization of fluctuations in granular hopper flow. *Granular Matter*. 2013;15(6):827-840.
31. Zhou Y, Wang H, Zhou B, Li J. DEM-aided direct shear testing of granular sands incorporating realistic particle shape. *Granular Matter*. 2018;20(3):55.
32. Ferellec J, McDowell G. Modelling realistic shape and particle inertia in DEM. *Géotechnique*. 2010;60(3):227.
33. O'Sullivan C. *Particulate Discrete Element Modelling: A Geomechanics Perspective*. New York: Taylor & Francis; 2011.
34. Lim K-W, Andrade JE. Granular element method for three-dimensional discrete element calculations. *Int J Numer Anal Methods Geomech*. 2014;38(2):167-188.
35. Kawamoto R, Andò E, Viggiani G, Andrade JE. Level set discrete element method for three-dimensional computations with triaxial case study. *J Mech Phys Solids*. 2016;91:1-13.

36. Kawamoto R, Andò E, Viggiani G, Andrade JE. All you need is shape: predicting shear banding in sand with LS-DEM. *J Mech Phys Solids*. 2018;111:375-392.

37. Zhao S, Evans TM, Zhou X. Random packing of tetrahedral particles using the polyhedral and multi-sphere discrete element method. In: Li X, Feng Y, Mustoe G, eds. *Proceedings of the 7th International Conference on Discrete Element Methods*. Singapore: Springer; 2016:91-99.

38. Katagiri J. A novel way to determine number of spheres in clump-type particle-shape approximation in discrete-element modelling. *Géotechnique*. 2018:1-7.

39. Lee SJ, Hashash YM, Nezami EG. Simulation of triaxial compression tests with polyhedral discrete elements. *Comput Geotech*. 2012;43:92-100.

40. Nezami EG, Hashash YM, Zhao D, Ghaboussi J. Shortest link method for contact detection in discrete element method. *Int J Numer Anal Methods Geomech*. 2006;30(8):783-801.

41. Boon C, Houlsby G, Utili S. A new algorithm for contact detection between convex polygonal and polyhedral particles in the discrete element method. *Comput Geotech*. 2012;44:73-82.

42. Ng T-T. Particle shape effect on macro- and micro-behaviors of monodisperse ellipsoids. *Int J Numer Anal Methods Geomech*. 2009;33(4):511-527.

43. Nguyen HBK, Rahman MM, Fourie AB. Undrained behaviour of granular material and the role of fabric in isotropic and K0 consolidations: DEM approach. *Géotechnique*. 2016;67(2):153-167.

44. Kuhn MR, Sun W, Wang Q. Stress-induced anisotropy in granular materials: fabric, stiffness, and permeability. *Acta Geotechnica*. 2015;10(4):399-419.

45. Wellmann C, Lillie C, Wriggers P. A contact detection algorithm for superellipsoids based on the common-normal concept. *Eng Comput*. 2008;25(5):432-442.

46. Peters JF, Hopkins MA, Kala R, Wahl RE. A poly-ellipsoid particle for non-spherical discrete element method. *Eng Comput*. 2009;26(6):645-657.

47. Zhang B, Regueiro RA, Druckrey A, Alshibli K. Construction of poly-ellipsoidal grain shapes from SMT imaging on sand, and the development of a new DEM contact detection algorithm. *Eng Comput*. 2018;35(2):733-771.

48. Lourakis MI. A brief description of the Levenberg-Marquardt algorithm implemented by Levmar. *Found Res Technol*. 2005;4(1):1-6.

49. Gilbert EG, Johnson DW, Keerthi SS. A fast procedure for computing the distance between complex objects in three-dimensional space. *IEEE J Rob Autom*. 1988;4(2):193-203.

50. Barr AH. Superquadrics and angle-preserving transformations. *IEEE Comput Graphics Appl*. 1981;1(1):11-23.

51. Williams JR, Pentland AP. Superquadrics and modal dynamics for discrete elements in interactive design. *Eng Comput*. 1992;9(2):115-127.

52. Agarwal S, Mierle K, Others. Ceres Solver. http://ceres-solver.org

53. Wächter A, Biegler LT. On the implementation of an interior-point filter line-search algorithm for large-scale nonlinear programming. *Math Program*. 2006;106(1):25-57.

54. Alonso-Marroquín F, Wang Y. An efficient algorithm for granular dynamics simulations with complex-shaped objects. *Granular Matter*. 2009;11(5):317-329.

55. Rapaport DC. *The Art of Molecular Dynamics Simulation—Second Edition*. London: Cambridge University Press; 2004.

56. Fincham D. Leapfrog rotational algorithms. *Mol Simul*. 1992;8(3-5):165-178.

57. van den Bergen G. Efficient collision detection of complex deformable models using AABB trees. *J Graphics Tools*. 1997;2(4):1-13.

58. Johnson K. *Contact Mechanics*. London: Cambridge University Press; 1985.

59. Van Den Bergen G. *Collision Detection in Interactive 3D Environments*. San Francisco: CRC Press; 2003.

60. Zhao S, Evans T, Zhou X. Effects of curvature-related DEM contact model on the macro- and micro-mechanical behaviours of granular soils. *Géotechnique*. 2018;68(12):1085-1098.

61. Šmilauer V, Catalano E, Chareyre B, et al. YADE reference documentation. http://yade-dem.org/doc/; 2010.

62. Delaney GW, Cleary PW. The packing properties of superellipsoids. *EPL (Europhys Lett)*. 2010;89(3):34002.

63. Christoffersen J, Mehrabadi MM, Nemat-Nasser S. A micromechanical description of granular material behavior. *J Appl Mech*. 1981;48(2):339-344.